scientific reports

Check for updates

OPEN

Integrative network pharmacology and multi-omics reveal anisodamine hydrobromide's multi-target mechanisms in sepsis

Ying Chen[1,2,4], Danlei Weng[1,4], Wei Shi[1], Shuxing Wei[1], Wenqing Ji[1], Xiya Wang[1], Yali Xu[1], Xiaoman Wang[3], Xue Mei[1]✉ & Shubin Guo[1]✉

Sepsis, marked by hyperinflammation and subsequent immunosuppression, lacks effective phase-specific therapies. Although anisodamine hydrobromide (Ani HBr) reduced 28-day mortality in our prior trial, its mechanisms remained unclear. Here, we integrated network pharmacology, machine learning, immunological profiling, molecular simulations, and single-cell transcriptomics to elucidate Ani HBr's multi-target actions. Among 30 cross-species targets, ELANE and CCL5 emerged as core regulators via protein interaction networks, survival modeling (AUC: 0.72–0.95), and statistical significance ($p < 0.05$). Ani HBr inhibited ELANE-driven NET formation (HR = 1.176), associated with immunosuppression and endothelial damage, while enhancing CCL5-related cytotoxic T-cell recruitment (HR = 0.810). Docking and dynamics simulations showed Ani HBr binds ELANE's catalytic cleft, suggesting direct inhibition of its enzymatic activity, and interacts stably with CCL5 at potential receptor-binding interfaces, indicating a modulatory role. Single-cell analysis revealed ELANE upregulation in CCI-phase neutrophils and widespread yet stage-specific CCL5 expression. These findings support Ani HBr as a phase-tailored agent that targets ELANE in early hyperinflammation while preserving CCL5-mediated immunity. The ELANE/CCL5 prognostic model offers a framework for precision immunotherapy in sepsis.

Sepsis is increasingly viewed as a complex immunometabolic syndrome in which a dysregulated host response drives organ injury and dysfunction[1,2]. An early hyperinflammatory phase ,driven by cytokines such as TNF-α, IL-1β and IL-6, often gives way to profound immunosuppression and metabolic dysregulation[3,4]. Metabolic byproducts play active signaling roles: for example, lactate accumulates during sepsis and feeds back on immune cells. Lactate transporters MCT1 and MCT4 and the lactate receptor GPR81 mediate immunosuppressive signals[5]. At the same time, sepsis induces mitochondrial dysfunction and ion channel perturbations[6]. For instance, opening the mitochondrial ATP-sensitive K^ + channel (mitoK_ATP) has been reported to attenuate inflammation in sepsis models[7]. These interwoven immune–metabolic–microenvironmental perturbations underscore why sepsis outcomes are hard to predict and why effective therapies remain elusive.

Anisodamine hydrobromide (Ani HBr), a belladonna alkaloid isolated from Solanaceae plants and synthesized in 1975, has demonstrated clinical efficacy in reducing 28-day mortality in septic shock patients[8]. While its microcirculatory benefits (endothelial stabilization, platelet inhibition) are well-documented[9,10], Ani HBr's immunomodulatory mechanisms remain elusive. Emerging evidence suggests Ani HBr ameliorates sepsis via multi-target actions: (1) suppressing neutrophil extracellular trap (NET) formation by inhibiting NLRP3 inflammasome activation[11]; (2) enhancing cytotoxic T-cell recruitment through chemokine signaling[12]; and (3) stabilizing endothelial glycocalyx to mitigate vascular leakage[13]. However, no studies have systematically linked these effects to specific gene networks or clinical stratification.

To address this knowledge gap, we adopted a systems-level strategy that leverages complementary computational experiment. Network pharmacology was first applied to reconstruct a comprehensive drug–target–gene–pathway network for AniHBr. This approach is well suited to multi-component, multi-target agents, as it analyzes complex interaction networks rather than a single target[14,15]. Machine learning was employed

[1]Emergency Medicine Clinical Research Center, Beijing Key Laboratory of Cardiopulmonar Cerebral Resuscitation, Beijing Chaoyang Hospital, Affiliated to Capital Medical University, Beijing 100020, China. [2]National Institute for Data Science in Health and Medicine, Capital Medical University, Beijing 100069, China. [3]Department of Rehabilitation, Shenzhen Dapeng New District Nan'ao People's Hospital, Shenzhen 518121, China. [4]Ying Chen and Danlei Weng contributed equally to this. ✉email: meixue96@163.com; shubin007@yeah.net

on high-dimensional transcriptomic and clinical datasets to identify prognostic biomarkers and key genes associated with sepsis severity. Modern machine learning algorithms excel at extracting informative features from genome-wide expression data and can suggest candidate therapeutic targets[16,17]. Molecular dynamics (MD) simulations with end-point MM-PBSA free-energy calculations were then used to validate and quantify predicted AniHBr–protein interactions. Since experimental determination of ligand–protein binding can be challenging, in silico MD provides a practical complement[18,19]. Single-cell RNA sequencing was utilized to resolve the cellular heterogeneity of the immune response. Single-cell analysis can reveal distinct subpopulations and states that are differentially regulated[20], such single-cell resolution makes it possible to trace how AniHBr might shift specific immune cell subsets or their metabolic states during sepsis.

In this study, network pharmacology systematically maps predicted drug–target–pathway interactions, identifying candidate proteins and signaling modules relevant to sepsis. Machine learning analyzes large-scale omics and clinical datasets to construct a sepsis prognostic model, through which it identifies key outcome-associated genes and thus enhances the precision of predicting compound–target interactions. Molecular dynamics simulations are used to validate predicted interactions by simulating Ani HBr binding to candidate targets and assessing the stability of the drug–protein complex over time. Single-cell RNA sequencing provides cellular context by revealing which immune subsets express the targets and how sepsis perturbs their states. Together, these methods test the hypothesis that Ani HBr modulates the ELANE–CCL5 axis—a dual regulatory node linking neutrophil elastase-driven NETosis (ELANE) and adaptive chemokine signaling (CCL5)—to reconcile sepsis's dysregulated immune response. By linking systems-level target discovery and cell-specific expression profiles with molecular binding validation, this integrative pipeline bridges mechanistic insight and personalized prognostic modeling, ultimately informing targeted therapeutic strategies.

Methods

Identification of Ani HBr-sepsis intersecting genes

Sepsis-related genes were curated from GEO[21] (GSE65682; sepsis vs. healthy controls) and GeneCards[22] (score ≥ 0.5). Differentially expressed genes (DEGs) were identified using the limma R package (v4.4.1; adjusted $p < 0.05$, |fold change| > 1). Ani HBr targets were predicted via Swiss Target Prediction[23], SuperPred[24], PharmMapper[25], TargetNet[26], and SEA[27] databases using its PubChem[28]-derived SMILES (CID: 118856046). Intersecting genes between Ani HBr targets, sepsis DEGs, and GeneCards-derived sepsis genes were identified using Venn analysis.

Functional enrichment analysis

Gene Ontology[29] (GO; biological process, cellular component, molecular function) and Kyoto Encyclopedia of Genes and Genomes[30] (KEGG) pathway analyses were performed using clusterProfiler package[31] in R. Terms with adjusted $p \leq 0.05$ (GO) or $p \leq 0.05$ (KEGG) were considered significant.

Protein–protein interaction (PPI) network construction

The STRING database[32] (confidence score > 0.7) was used to construct PPI networks, visualized and analyzed in Cytoscape[33] (v3.10.2). Hub genes were identified via the CytoHubba[34] plugin using maximal clique centrality (MCC) algorithm, selecting the top seven ranked genes.

Machine learning-based prognostic modeling

A cohort of 479 sepsis patients (GSE65682) was randomly split into training (70%) and validation (30%) sets. Ten algorithms (RSF, Enet, StepCox, etc.) with 117 combinations were evaluated using the Mime R package[35]. Model performance was assessed via Harrell's C-index, with the optimal model (StepCox[forward] + RSF) selected based on highest average C-index. To further elucidate how each selected feature gene contributes to the model's predictive performance, we employed the survex R package and applied the SurvLIME method for feature-importance evaluation. SurvLIME constructs a local surrogate Cox proportional-hazards model around each observation, approximating the complex survival model in its immediate neighborhood, and then uses the surrogate's coefficients to quantify the importance of each variable[36]. By attributing a clear contribution score to each gene, this approach enhances the interpretability of our prognostic model..

Survival analysis

Three prognostic genes were identified by intersecting PPI hub genes with machine learning-derived features. Univariate Cox regression ($p < 0.05$) and Kaplan–Meier analysis (log-rank test) assessed survival associations. Multivariate Cox regression ($p < 0.05$) identified prognostic targets.

Risk score model development

A risk score (RS)[37] was calculated as: $RS = h_0(t) * \exp(\beta_1\chi_1 + \beta_2\chi_2 + \cdots + \beta_n\chi_n)$, where β_n represents the Cox regression coefficient for each gene, χ_n denotes the log2-transformed normalized expression value of the corresponding gene, and $h_0(t)$ is baseline hazard function. Patients were stratified into high/low-risk groups using RS. Model performance was validated via time-dependent ROC curves (AUC), Kaplan–Meier survival, and nomogram-based 7-/14-/28-day mortality prediction. Decision curve analysis (DCA) quantified clinical net benefit.

Immune profiling and checkpoint analysis

We applied the CIBERSORT algorithm[38] via the immunedeconv R package[39] to the GSE65682 gene expression dataset, using the LM22 signature matrix to quantify the relative abundance of 22 immune cell subpopulations. Patients were stratified into high- and low-risk groups according to the ELANE/CCL5-derived RS, and differences

in immune cell infiltration between these groups were assessed by Student's t-test ($p < 0.05$). Next, we downloaded a panel of 50 experimentally validated immune checkpoint genes (inhibitory molecules such as PD-1, CTLA-4, TIM-3 and co-stimulatory molecules such as CD28, ICOS) from the ImmPort database[40] and intersected this list with sepsis differentially expressed genes to identify 29 significantly dysregulated checkpoints—among them PD-L1 (CD274), TIM-3 (HAVCR2), LAG3, and CD28. Finally, we compared checkpoint gene expression between high- and low-risk groups and evaluated the correlation between RS and checkpoint expression using Spearman's rank correlation.

Molecular docking

The 3D structure of Ani HBr (PubChem CID 118,856,046)[28] was downloaded from PubChem (accessed Jan 24, 2025), converted from SDF to MOL2 via Open Babel GUI, and prepared in AutoDock Tools by defining the root atom, setting rotatable bonds, adding Gasteiger charges and polar hydrogens, then saving as PDBQT. Protein structures were retrieved from the Protein Data Bank (accessed May 28, 2025): ELANE (PDB ID: 5ABW, chain A; resolution 1.60 Å) and CCL5 (PDB ID: 5CMD; resolution 3.09 Å)[41]. Structures were prepared in PyMOL by removing crystallographic waters and ligands and exporting as clean PDB files. Using AutoDock Tools, polar hydrogens were added and nonpolar hydrogens merged on both protein and ligand structures, and ligand rotatable bonds were defined. For ELANE (5ABW), the docking grid was centered at ($x = 16.25$, $y = -27.09$, $z = 0.40$) with box dimensions of $39.75 \times 42.00 \times 38.25$ Å; for CCL5 (5CMD), the grid was centered at ($x = -44.83$, $y = 25.87$, $z = -13.75$) with box dimensions of $47.25 \times 47.25 \times 47.25$ Å. Molecular docking was performed using AutoDock Vina 1.1.2 to predict protein–ligand binding poses. The lowest-energy conformations were selected based on Vina scoring, then visualized and analyzed in PyMOL and Discovery Studio 2019 to identify key interactions between Ani HBr and target residues.

Molecular dynamics simulation (MDS)

Molecular dynamics (MD) simulations were carried out using GROMACS 2022. Protein and ligand topologies were generated via the pdb2gmx tool (CHARMM36[42] force field for ELANE/CCL5) and the AutoFF web server (CGenFF parameters for Ani HBr), respectively. Each complex was solvated in a cubic TIP3P water box with a 1.0 nm buffer[43], and neutralized by adding counter-ions via gmx genion. Long-range electrostatics were treated with the Particle Mesh Ewald (PME) method (cutoff = 1.0 nm), and all bonds were constrained using the LINCS algorithm. Simulations employed the leap-frog (Verlet) integrator with a 1 fs timestep. Prior to dynamics, each system underwent energy minimization by the steepest-descent algorithm (3,000 steps), followed by position-restrained minimizations in three stages: (1) restraining the protein/ligand heavy atoms while relaxing solvent; (2) restraining counter-ions while relaxing the rest of the system; and (3) unrestrained minimization of all atoms. Production runs were performed in the isothermal–isobaric (NPT) ensemble at 310 K and 1 bar for 100 ns, with temperature and pressure maintained using the velocity-rescaling thermostat and Parrinello–Rahman barostat, respectively. Trajectory analyses—including root-mean-square deviation (RMSD), root-mean-square fluctuation (RMSF), hydrogen bonds, radius of gyration (Rg), and solvent-accessible surface area (SASA)—were computed using gmx rms, gmx rmsf, gmx hbond, gmx gyrate, and gmx sasa. Finally, binding free energies of each protein–ligand complex were estimated via the g_mmpbsa tool implementing the MM-PBSA method.

Single cell analysis

Single-cell RNA-seq data (GSE175453) were retrieved from GEO, comprising five healthy controls and four sepsis patients (one rapidly recovering [RAP], three chronic critical illness [CCI]) with peripheral blood myeloid-enriched and PBMC mixtures. Data were processed in Scanpy[44]: cells with < 300 detected genes, > 20% mitochondrial reads, or outlier ribosomal/hemoglobin expression were removed, and genes expressed in < 5 cells were excluded. Counts were normalized to 10,000 UMIs per cell and $\log_{10}$-transformed. The top 2,000 highly variable genes were identified, and PCA was performed on these features, retaining 50 principal components. Harmony corrected batch effects on these PCs before constructing a k-nearest neighbor graph ($k = 20$) using the first 15 Harmony-adjusted PCs. Leiden clustering (resolution = 1.6) defined cell communities, which were visualized by UMAP. Automated annotation via CellTypist's[45] immune reference was refined manually using canonical markers, identifying major myeloid, lymphoid, and rare cell types. Monocle 3 pseudotime analysis[46], using classical monocytes as the root, ordered cells along inferred trajectories and calculated entropy to reveal dynamic differentiation and branching during sepsis progression.

Results

Identification of intersecting genes in Ani HBr and sepsis

Figure 1 outlines the overall workflow of the study. Figure 2 displays the collection of Ani HBr target genes derived from five databases, resulting in a set of 484 Ani HBr-related genes. Using k-means clustering on the PPI network derived from STRING, the 484 genes were grouped into five clusters (Supplementary Figure S1). To ensure the quality of the GSE65682 dataset, a heatmap, volcano plot, and PCA plot were generated (Supplementary Figure S2). We identified 975 differentially expressed genes associated with sepsis and retrieved 3,010 sepsis-related target genes from the GeneCards database. The intersection of these datasets yielded 30 intersecting genes, as depicted in the Venn diagram (Fig. 3A). Figure 3B shows a heatmap comparing the expression levels of these 30 genes among sepsis survivors, non-survivors, and healthy individuals. For example, genes such as FKBP1B, ARG1, and CTSD exhibit elevated expression in sepsis patients compared to healthy controls, whereas genes such as STAT1, PDE4B, and CFD display reduced expression in sepsis. Notably, these differences are consistent across survivors and non-survivors. Figure 3C illustrates the correlation matrix among these 30 genes, highlighting strong positive correlations between ELANE and CTSG, as well as MMP9 and

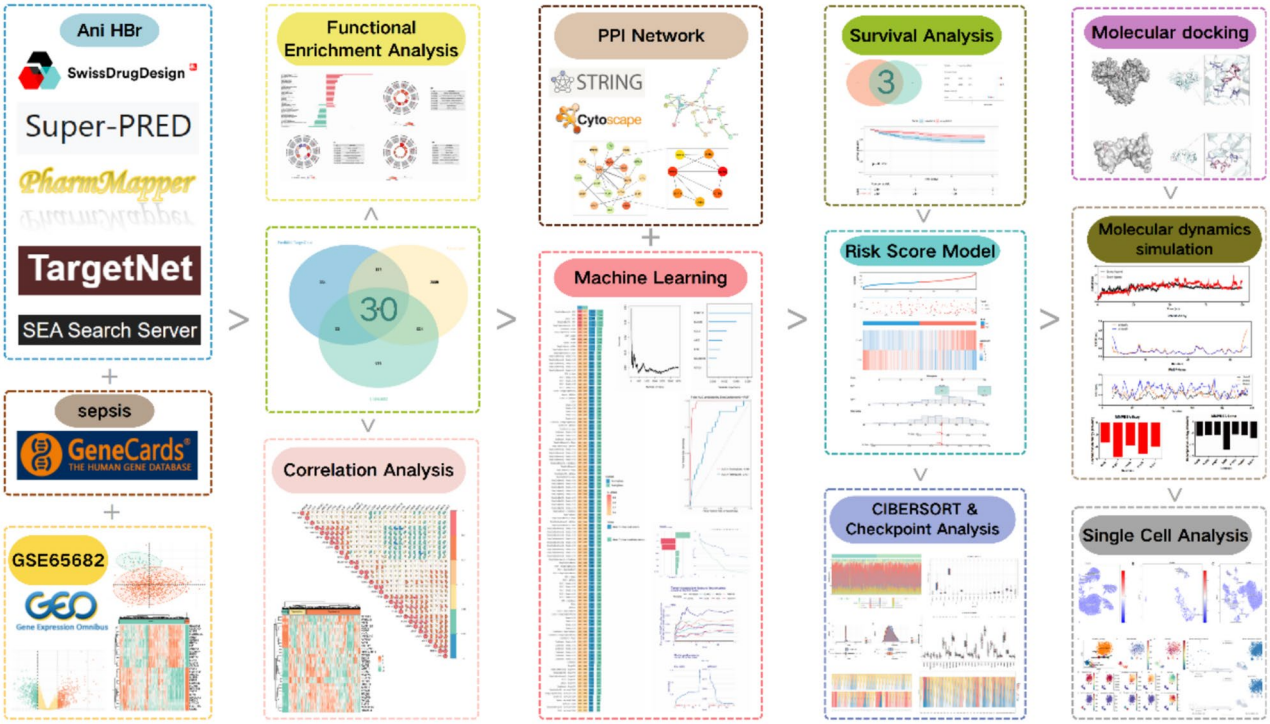

Fig. 1. The overall workflow of the study.

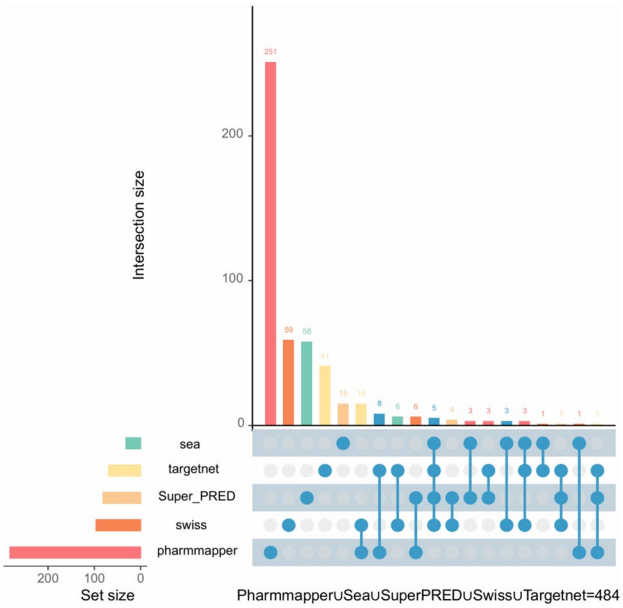

Fig. 2. Ani HBr targets were predicted using five databases: Swiss Target Prediction, Super-PRED, PharmMapper, TargetNet, and SEA. The union of the predicted targets from these databases resulted in a total of 484 genes.

ARG1, which suggests possible co-regulation and functional relatedness. Conversely, AKR1B1 shows strong negative correlations with MAPK14 and TLR8, implying potential antagonistic roles in sepsis pathophysiology.

Gene ontology (GO) and KEGG pathway enrichment analysis of intersecting genes

The 30 intersecting genes were subjected to GO and KEGG enrichment analyses. KEGG pathway analysis (Fig. 4) indicate that elevated ELANE expression is associated with pathological activation of pathways such as NETosis, IL-17 signaling, TLR, and TNF, which together perpetuate a "inflammation-damage-reinflammation" vicious

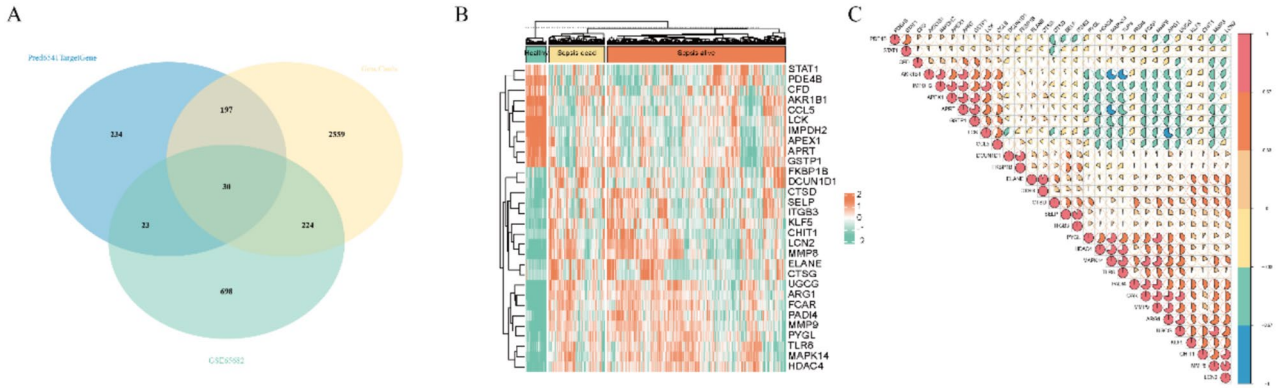

Fig. 3. Intersection and Expression Analysis of Ani HBr Targets, GeneCards Sepsis Genes, and DEGs (**A**) Venn diagram of Ani HBr targets (blue), GeneCards–derived sepsis genes (yellow), and DEGs from GSE65682 (green), identifying 30 overlapping genes, including STAT1, PDE4B, and CFD. (**B**) Heatmap of the 30 intersecting genes across healthy controls (left), non-survivor sepsis patients (middle), and survivor sepsis patients (right); red and green indicate high and low expression, respectively. (**C**) Pairwise correlation analysis among key genes: each tile represents the correlation between two genes, with red indicating positive correlation and blue indicating negative correlation; color intensity corresponds to the strength of the correlation (e.g., ELANE–CTSG and MMP9–ARG1 show strong positive associations, whereas AKR1B1–MAPK14 and AKR1B1–TLR8 are negatively correlated).

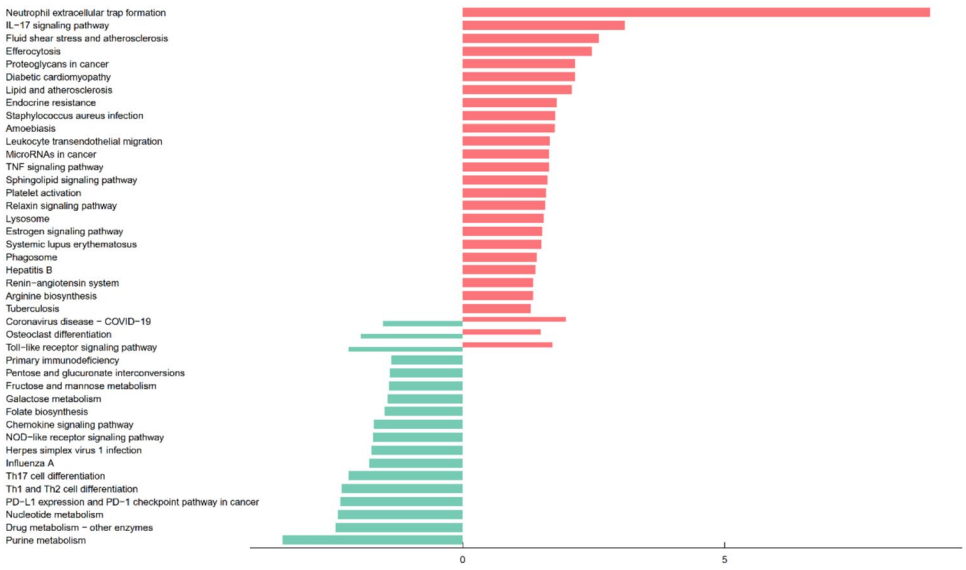

Fig. 4. KEGG pathway enrichment analysis of the 30 intersecting genes, with red bars representing upregulated genes and green bars representing downregulated genes.

cycle in sepsis. This cycle significantly increases mortality risk. In contrast, low CCL5 expression correlates with inhibition of chemokine signaling, impaired Th1 differentiation, and metabolic defects such as purine metabolism, nucleotide metabolism and folate biosynthesis. Downregulation of these pathways contributes to failed immune cell recruitment (due to insufficient CCL5) and persistent immune suppression (due to T-cell and NK cell dysfunction). GO biological process (GO-BP) analysis (Fig. 5A) highlighted responses to lipopolysaccharide and bacterial-derived molecules, while GO cellular component (GO-CC) analysis (Fig. 5B) indicated enrichment in processes related to ribonucleotide metabolism. GO molecular function (GO-MF) analysis (Fig. 5C) showed associations with specific granules. Collectively, these pathways regulate immune responses, inflammation, and cellular responses to pathogens (e.g., bacteria and viruses) and encompass both innate (e.g., TLR signaling, NOD-like receptor signaling, leukocyte migration, and chemotaxis) and adaptive immune mechanisms (e.g., T cell differentiation, PD-1/PD-L1 pathway), in addition to processes related to organelle function, metabolism, and extracellular matrix remodeling. Together, these biological processes underpin the body's defense against pathogens while playing crucial roles in inflammation, immune regulation, and tissue repair.

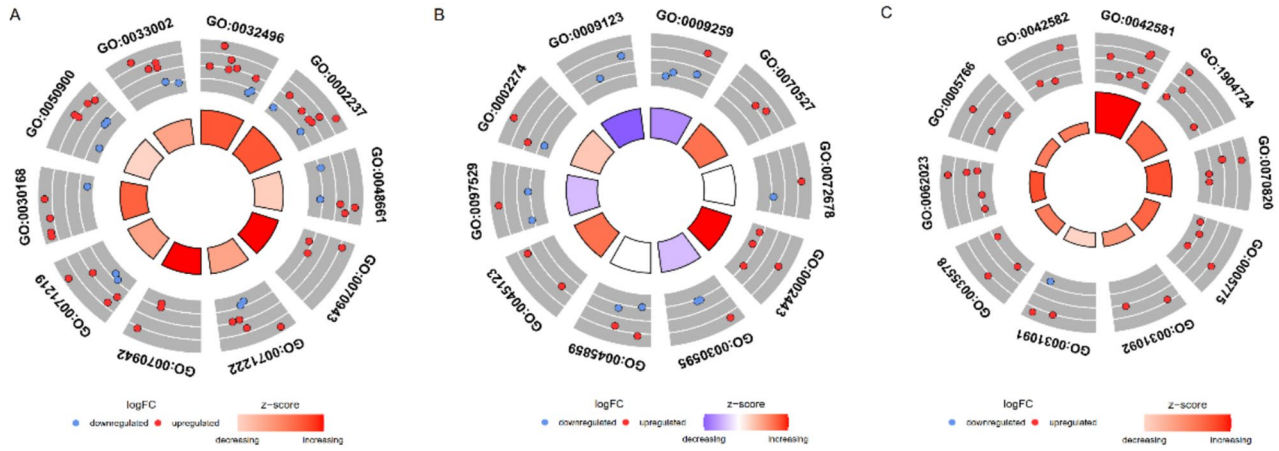

ID	Description
GO:0032496	response to lipopolysaccharide
GO:0002237	response to molecule of bacterial origin
GO:0048661	positive regulation of smooth muscle cell proliferation
GO:0070943	neutrophil-mediated killing of symbiont cell
GO:0071222	cellular response to lipopolysaccharide
GO:0070942	neutrophil mediated cytotoxicity
GO:0071219	cellular response to molecule of bacterial origin
GO:0030168	platelet activation
GO:0050900	leukocyte migration
GO:0033002	muscle cell proliferation

ID	Description
GO:0009259	ribonucleotide metabolic process
GO:0070527	platelet aggregation
GO:0072678	T cell migration
GO:0002443	leukocyte mediated immunity
GO:0030595	leukocyte chemotaxis
GO:0045859	regulation of protein kinase activity
GO:0045123	cellular extravasation
GO:0097529	myeloid leukocyte migration
GO:0002274	myeloid leukocyte activation
GO:0009123	nucleoside monophosphate metabolic process

ID	Description
GO:0042581	specific granule
GO:1904724	tertiary granule lumen
GO:0070820	tertiary granule
GO:0005775	vacuolar lumen
GO:0031092	platelet alpha granule membrane
GO:0031091	platelet alpha granule
GO:0035578	azurophil granule lumen
GO:0062023	collagen-containing extracellular matrix
GO:0005766	primary lysosome
GO:0042582	azurophil granule

Fig. 5. (**A**–**C**) GO enrichment analysis of the 30 intersecting genes across Biological Processes (BP), Cellular Components (CC), and Molecular Functions (MF), respectively, depicted as dot plots where each dot represents a gene.

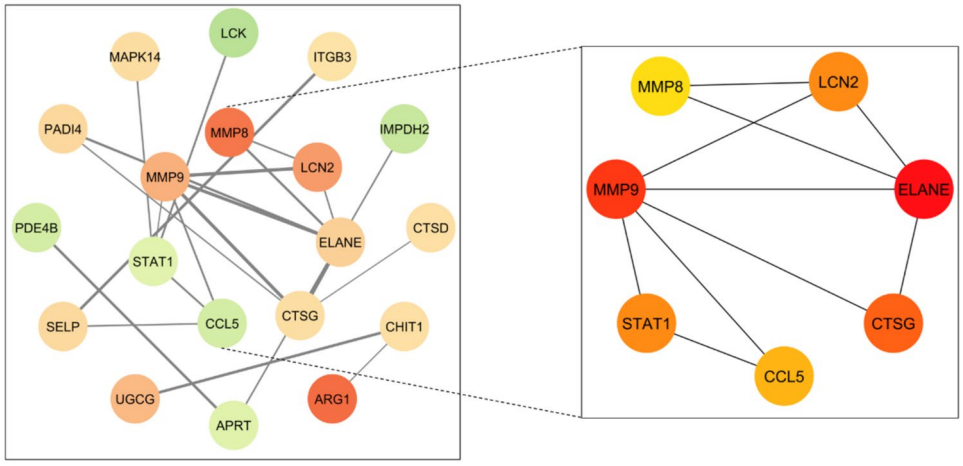

Fig. 6. Identification of key genes using the CytoHubba plugin, resulting in the selection of 7 hub genes.

PPI analysis for identifying key genes related to Ani HBr and sepsis

The protein–protein interaction (PPI) network constructed using the STRING database (interaction score > 0.7) comprised 19 nodes and 21 edges (Supplementary Figure S3); 11 genes did not interact with others. Using the Cytoscape CytoHubba plug-in with the MCC algorithm, the top seven hub genes—CCL5, LCN2, CTSG, MMP9, MMP8, ELANE and STAT1—were identified (Fig. 6).

Machine learning for identifying key genes related to Ani HBr and sepsis

To identify key genes influencing 28-day survival, we selected 479 sepsis patients and divided them into training and validation cohorts based on the 30 intersecting genes. In the training cohort, 117 algorithm combinations were fitted using the "Mime" R package to construct a prognostic model, and the average C-index was calculated for each algorithm in internal validation (Supplementary Fig. S4). When C-index values were similar, models with fewer hub genes were preferred. As a result, the StepCox[forward] + RSF combination was selected as the final model, achieving a C-index of 0.95 in the training set and 0.7 in the validation set, both demonstrating

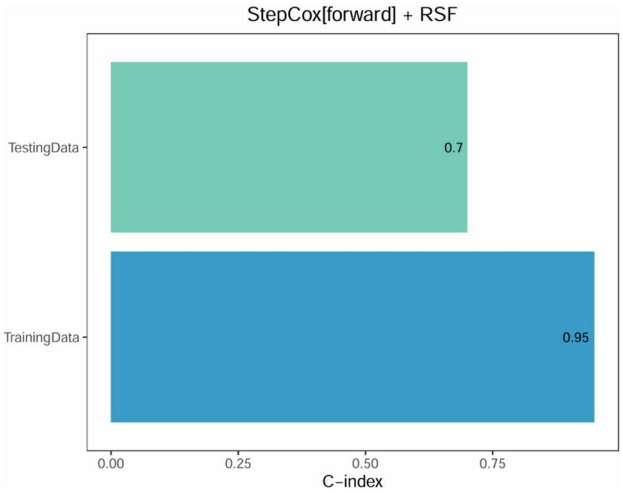

Fig. 7. Concordance index (C-index) of the StepCox[forward] + RSF model in the training (blue) and validation (green) cohorts, showing C-indices of 0.95 and 0.70, respectively, with calibration indicating good model performance.

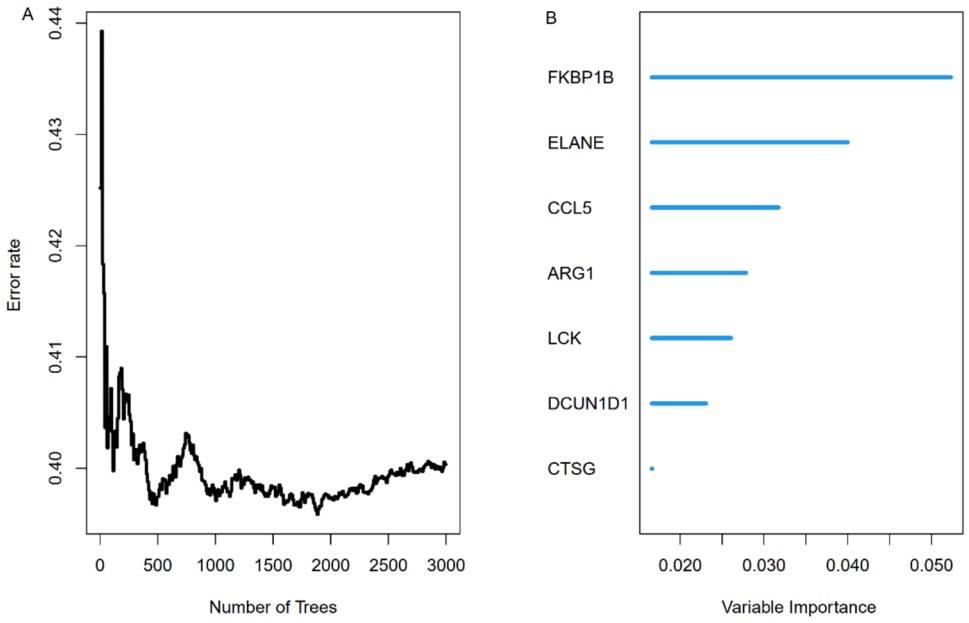

Fig. 8. Error Rate and Feature Importance of the StepCox[forward] + RSF Model (**A**) Out-of-bag error rate across 3,000 trees in the validation cohort, with a minimum error of 0.30. (**B**) Importance ranking of the seven selected genes—FKBP1B, ELANE, CCL5, ARG1, LCK, DCUN1D1, and CTSG—where higher scores indicate greater contribution to model performance.

good calibration (Fig. 7). Figure 8A illustrates the trend of the out-of-bag (OOB) error rate, which stabilizes when ntree > 1000. Figure 8B ranks the importance of the seven genes selected by StepCox[forward] + RSF, with FKBP1B, ELANE, and CCL5 identified as the top three. The model was then used to predict 7-day, 14-day, and 28-day mortality in the validation cohort, with AUC values of 0.737, 0.734, and 0.72, respectively (Supplementary Fig. S5). Figure 9 provides a time-dependent interpretation of the selected genes. Figure 9A presents a local explanation for a specific patient, showing the daily influence of the seven genes on 28-day survival predictions since admission. We utilized the SurvLIME explanation method to analyze key feature importance and model predictive capabilities. Figure 9B combines model interpretability analysis of one patient subset. The left panel displays local feature importance derived from SurvLIME, while the right panel compares the survival functions of the black-box model and the SurvLIME explanation model. ARG1, CCL5, and LCK exhibit the highest local importance. ARG1 positively influences survival probability (green bars), whereas CCL5 and LCK show negative impacts (red bars), suggesting potential associations with adverse outcomes. The black-box

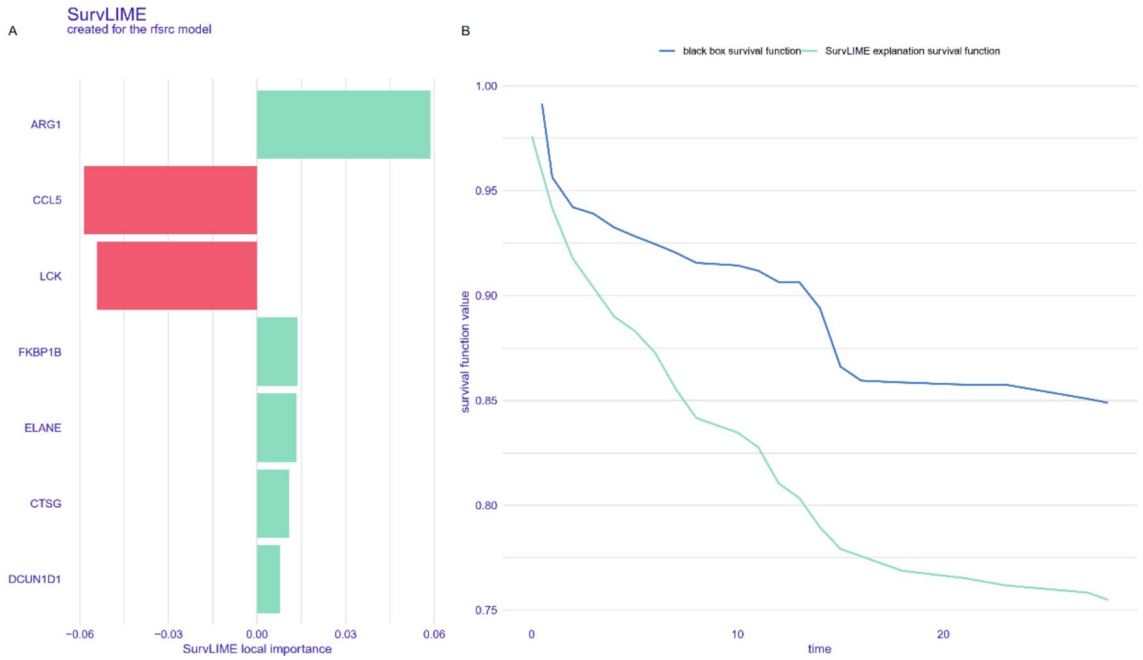

Fig. 9. Local Explanation of the StepCox[forward] + RSF Model (**A**) Local feature contributions for a representative patient, showing each gene's positive (green) or negative (red) impact on predicted 28-day mortality; ARG1 has the strongest positive effect, while CCL5 and LCK exert negative effects. (**B**) Comparison of the "black-box" RSF survival curve (blue) with the SurvLIME-explained survival function (green), both starting at 1.00 and declining over time, demonstrating that SurvLIME closely approximates the model's predictions.

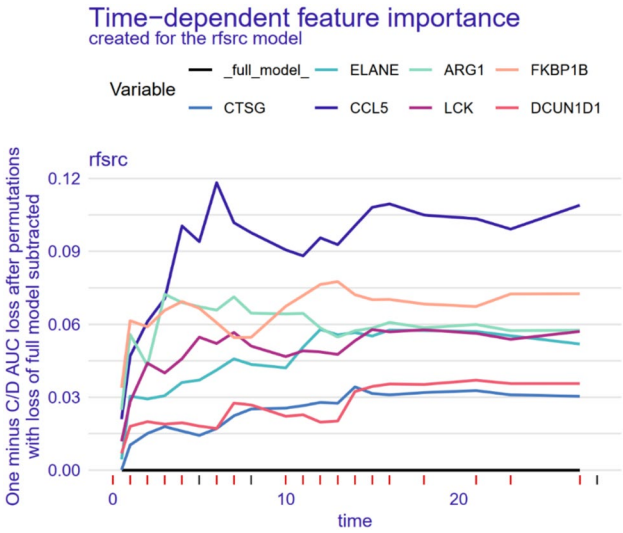

Fig. 10. Global, Time-Dependent Feature Importance of the StepCox[forward] + RSF Model Lines represent each gene's importance over time, measured by changes in dynamic AUC loss. CCL5 consistently shows the highest importance at all time points, with its influence increasing over the course of prediction. FKBP1B, LCK, ARG1, and ELANE also maintain high and stable importance, indicating their sustained contributions to survival risk estimation.

model (blue line) predicts higher survival probabilities, indicating its advantage in capturing complex nonlinear relationships. The SurvLIME explanation model (green line) predicts slightly lower survival probabilities but follows a similar trend, demonstrating that SurvLIME effectively captures key influencing factors and validates the reliability of feature importance. Figure 10 illustrates the time-dependent feature importance within the model. Feature importance is defined as "1 minus the C/D AUC loss," reflecting each feature's contribution

to the model's predictive performance across different time points. CCL5 consistently emerges as the most important feature, with its importance slightly increasing over time. This suggests its pivotal role in the model and potential relevance to inflammatory response and immune regulation. FKBP1B, LCK, ARG1 and ELANE also exhibit high and relatively stable importance, indicating sustained influence on survival predictions. Supplementary Figure S6 presents the model's predictive performance over time, assessed using the Brier Score and C/D AUC metrics. The Brier Score is low in the early time periods and increases in later stages but still lower than 0.5, indicating high predictive accuracy. The model's C/D AUC approaches 1 initially, reflecting excellent discriminative capacity. Although it decreases slightly over time, it stabilizes around 0.91, maintaining strong discriminative performance. These findings provide robust data support for the model's reliability and interpretability, demonstrating the effectiveness of machine learning approaches in survival analysis.

Identification of prognostic genes related to Ani HBr and sepsis (PGRAS) and construction of a risk score model

The intersection of the seven machine learning-selected genes with the seven hub genes yielded three key prognostic genes (Fig. 11A). Correlation analysis (Fig. 11B) revealed a strong positive correlation between ELANE and CTSG. Based on median expression levels, each gene was categorized into high- and low-expression groups. Univariate Cox regression analysis (Supplementary Fig. S7) confirmed the prognostic significance of these genes, and Kaplan–Meier survival analyses demonstrated significant survival differences between high- and low-expression groups (Supplementary Fig. S8). Through multivariate Cox regression(Supplementary Fig. S9) with stepwise selection ($p < 0.05$), ELANE ($p < 0.001$, HR = 1.176) and CCL5 ($p = 0.011$, HR = 0.810) were identified as the final prognostic genes. A risk score (RS) was computed based on their expression and coefficients, stratifying patients into high- and low-risk groups (Fig. 12). Consistent with the hazard ratios, high-risk patients exhibited elevated ELANE and reduced CCL5 expression, and these patients had significantly worse survival outcomes (Fig. 13). Cox regression confirmed RS as an independent prognostic factor, with the prognostic model showing AUC values of 0.64, 0.65, and 0.64 for 7-, 14-, and 28-day ROC curves, respectively (Supplementary Fig. S10). Additionally, RS and patient age were independently associated with overall survival (OS) in multivariate analysis(Supplementary Fig. S11), and these factors were incorporated into a nomogram for predicting 7-, 14-, and 28-day OS (Supplementary Fig. S12).

Landscape of immune infiltration of PGRAS

CIBERSORT with the LM22 signature was applied to deconvolve 22 immune cell subsets from GSE65682 bulk expression data (Supplementary Figure S13). Patients were stratified into high- and low-risk groups by ELANE/CCL5 risk score, retaining samples with $P < 0.05$ (Fig. 14). Two-sample t-tests ($\alpha = 0.05$) revealed significant enrichment of regulatory T cells (Tregs; $p = 0.02$) and monocytes ($p = 0.032$) in the high-risk cohort (Supplementary Figure S14). This pattern suggests compensatory monocyte recruitment coupled with Treg-mediated immunosuppression and a shift toward reparative (M2-like) monocyte phenotypes.

Landscape of immune checkpoints of PGRAS

Expression of 29 differentially expressed immune checkpoints was compared between high- and low-risk sepsis patients (Fig. 15A). In the low-risk group, most checkpoints—including TMIGD2, ICOS, PDCD1, TNFSF14, TNFRSF9/14/25, CD27/28/70, CD86, IDO1, LAG3, NCR3, and TIGIT—were upregulated, indicating a robust anti-pathogen response with potential T cell exhaustion. In contrast, ENTPD1 and LAIR1 levels were elevated in the high-risk group, consistent with enhanced immunosuppression. The risk score (RS) exhibited

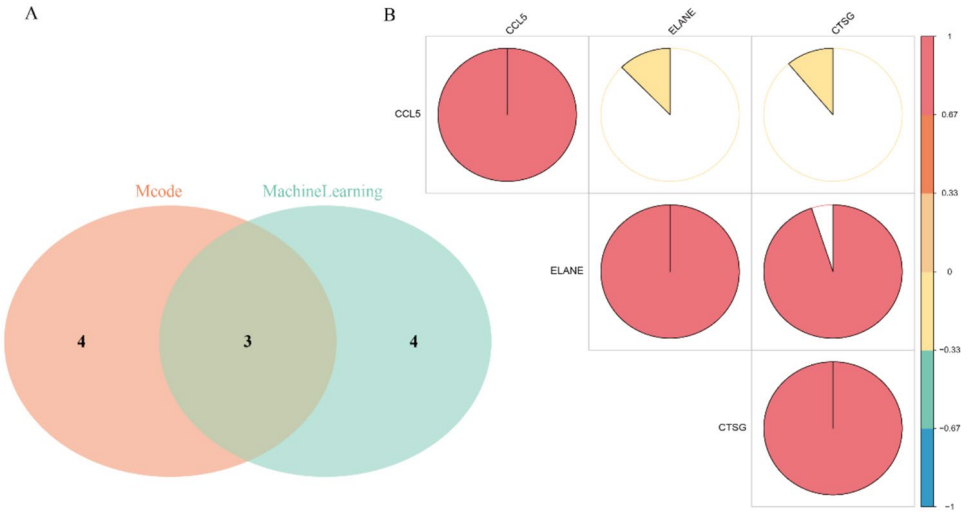

Fig. 11. (**A**) Venn diagram illustrating the intersection of genes identified through protein–protein interaction (PPI) network analysis and machine learning prognostic models, resulting in four key genes. (**B**) Correlation analysis among the 3 key genes.

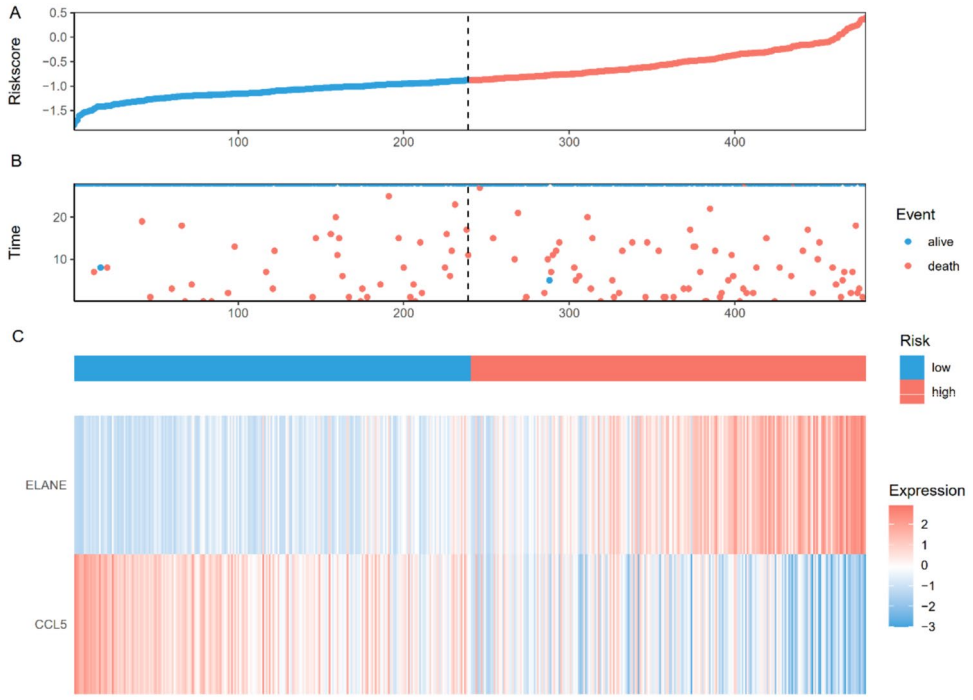

Fig. 12. Prognostic Risk Stratification by Key Genes (**A**) Individual risk scores ranked from lowest to highest; median cutoff (dashed line) separates low-risk (blue) and high-risk (red) groups. (**B**) Patient survival status versus risk score: blue dots indicate survivors, red dots indicate non-survivors, with a higher mortality rate in the high-risk group. (**C**) Expression of ELANE and CCL5 in low- versus high-risk groups, showing low-risk patients have low ELANE and high CCL5, whereas high-risk patients exhibit the opposite pattern.

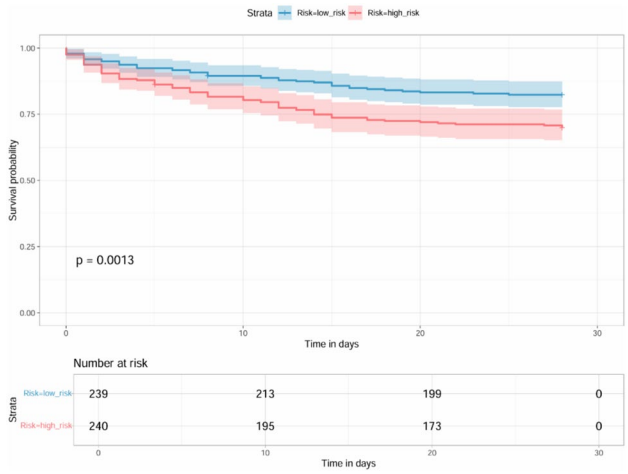

Fig. 13. Kaplan–Meier curve demonstrating the impact of the risk index on 28-day survival.

significant negative correlations with the majority of checkpoints (e.g., CD27/28/70, PDCD1, TIGIT, LAG3) and positive correlations with ENTPD1 and LAIR1 (Fig. 15B). Focusing on ELANE and CCL5 (Fig. 16), ELANE expression demonstrated inverse associations with CD160, CD274, CD44/48, HAVCR2, ICOS, IDO1, TIGIT, and various TNFRSF/TNFSF members, while correlating positively with CD27, suggesting a pro-inflammatory bias via downregulation of inhibitory pathways and upregulation of co-stimulatory signaling. Conversely, CCL5 displayed bidirectional correlations—positive with CD160, CD27/28/70, ICOS, LAG3, NCR3, PDCD1/PDCD1LG2, TIGIT, TMIGD2, TNFRSF9/14/25, and TNFSF14, and negative with CD274, CD44/48, ENTPD1, HAVCR2, and LAIR1—reflecting its dual role in promoting effector cell recruitment while modulating specific immunosuppressive checkpoints. These distinct correlation patterns underscore ELANE's and CCL5's unique contributions to the sepsis immune checkpoint milieu and highlight potential avenues for targeted immunomodulation.

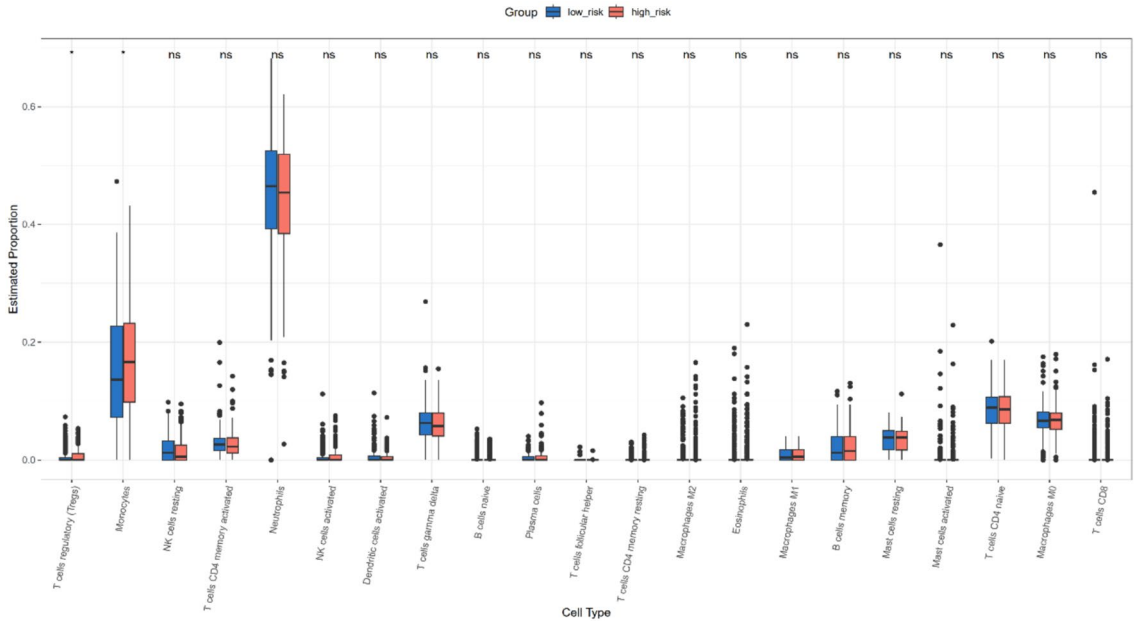

Fig. 14. Differential Immune Cell Infiltration Between Risk Groups Boxplots comparing the proportions of 22 immune cell subsets in high- (red) versus low-risk (blue) patients. "*" indicates $P < 0.05$; "ns" denotes no significant difference.

Molecular docking analysis

For ELANE, the best-scoring pose exhibited a binding energy of −6.1 kcal/mol. In this complex, Ani HBr's aromatic ring engages in a π–π stacking interaction with PHE192, while its tropane moiety packs against VAL216 through π–alkyl contacts. A network of van der Waals interactions stabilizes the ligand in the active-site cleft, involving residues PHE215, SER214, VAL62, PHE41, LEU99 and CYS58 (Fig. 17A). No direct hydrogen bonds were observed, suggesting that hydrophobic and aromatic contacts dominate Ani HBr's association with ELANE.

Docking against the CCL5 oligomer produced an even stronger predicted affinity (−7.6 kcal/mol). Here, Ani HBr forms a key hydrogen bond between its ester oxygen and the side-chain hydroxyl of THR7. A π-cation interaction with LYS33 further anchors the ligand, complemented by hydrophobic contacts from LYS33's aliphatic chain. Additional van der Waals interactions involve PRO9, PHE12, ALA13, SER5, SER31 and GLY32 (Fig. 17B). This constellation of polar and nonpolar contacts likely underlies the enhanced stability and tighter binding of Ani HBr to CCL5 compared with ELANE.

Together, these docking results identify critical residues that mediate Ani HBr's interactions with two key nodes of the ELANE/CCL5 axis. The differential binding affinities and interaction profiles provide a structural rationale for Ani HBr's dual modulation of NETosis and chemokine signaling in sepsis.

Molecular dynamics simulations

To assess the stability and dynamics of the Ani HBr–ELANE (5ABW) and Ani HBr–CCL5 (5CMD) complexes, we carried out 100 ns MD simulations in the NPT ensemble at 310 K and 1 bar. The root-mean-square deviation (RMSD) of the protein-ligand backbone atoms provides a measure of complex equilibration and stability (Fig. 18A). The 5CMD–Ani HBr complex equilibrated between 5 and 35 ns, oscillating around 0.25 nm, before gradually rising after 35 ns—indicative of a slight expansion of the binding interface. In contrast, the 5ABW–Ani HBr complex reached equilibrium within the first 5 ns and thereafter fluctuated by only ± 0.10 nm around an average RMSD of ~ 0.10 nm, demonstrating markedly higher conformational stability. The radius of gyration (Rg) tracks the overall compactness of each complex (Fig. 18B). The 5CMD–Ani HBr system maintained a stable Rg (~ 1.8 nm) until ≈40 ns, after which it gradually increased to ~ 1.9 nm, reflecting a modest loosening of the complex. By contrast, the 5ABW–Ani HBr complex exhibited minimal Rg fluctuations (~ 1.7 nm throughout), confirming that the Ani HBr–ELANE binding pocket remains tightly packed. Solvent-accessible surface area (SASA) calculations (Fig. 18C) showed that both complexes experienced only slight SASA fluctuations before settling into stable plateaus. This behavior suggests that Ani HBr binding induces minor adjustments in the local hydration shell but does not cause large-scale exposure or burial of surface residues. Hydrogen bonds between Ani HBr and its targets were monitored over the trajectory (Fig. 18D). The 5CMD complex formed between 0 and 6 H-bonds at any given time, averaging ~ 2 persistent hydrogen bonds. Similarly, the 5ABW complex maintained 0–5 H-bonds, also centering around ~ 2. These results indicate robust hydrogen-bond networks that contribute to ligand retention. Root-mean-square fluctuation (RMSF) profiles quantify per-residue flexibility (Fig. 19). In the 5ABW–Ani HBr complex, most residues exhibited RMSF values below 0.3 nm, indicating low flexibility and a rigid binding interface. The 5CMD–Ani HBr complex showed higher RMSF peaks (up to 1.0 nm) at several loop and surface regions, consistent with the greater overall mobility observed in RMSD and Rg analyses. Using

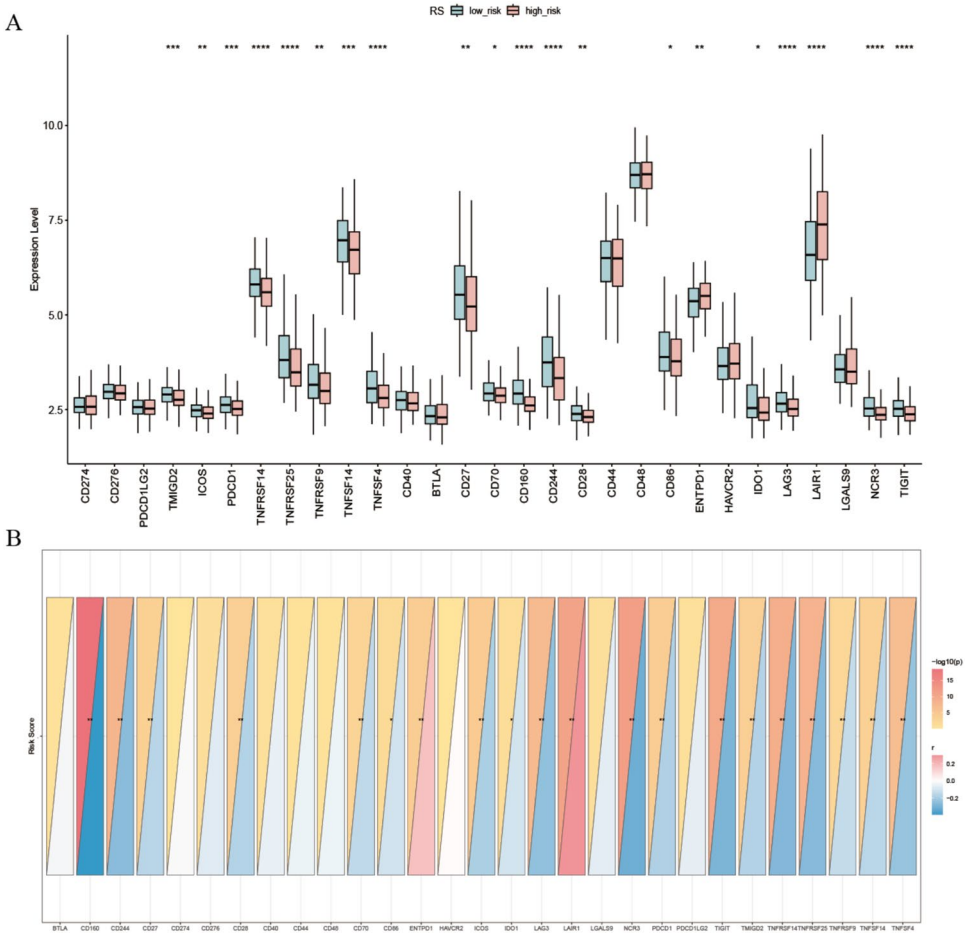

Fig. 15. Differences and Correlations Between Risk Score and Immune Checkpoint Genes. (**A**) Differential expression of 29 immune checkpoint genes between high- and low-risk groups. (**B**) Correlation between the risk score and each of the 29 immune checkpoint genes. Each rectangle represents the correlation strength (r) and significance (−log10 p). $p < 0.05$ (), < 0.01 (), < 0.001 (), < 0.0001 (****).

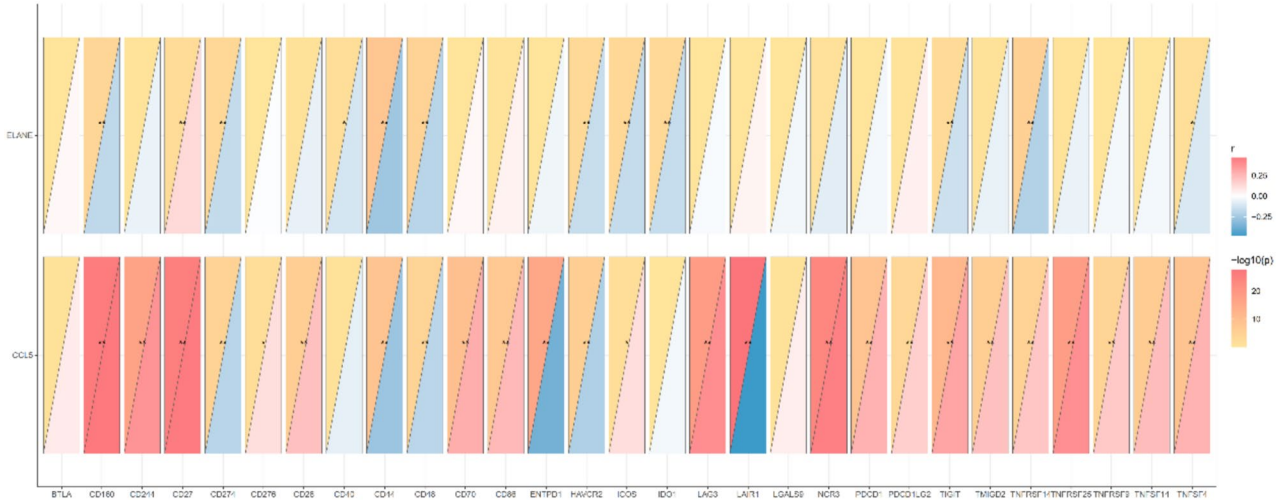

Fig. 16. Correlation Between ELANE/CCL5 Expression and Immune Checkpoint Genes. Heatmaps show the correlations between ELANE or CCL5 expression and 29 immune checkpoint genes. Each rectangle represents the correlation coefficient (r) and statistical significance (−log10 p). $p < 0.05$ (*), $p < 0.001$ (**).

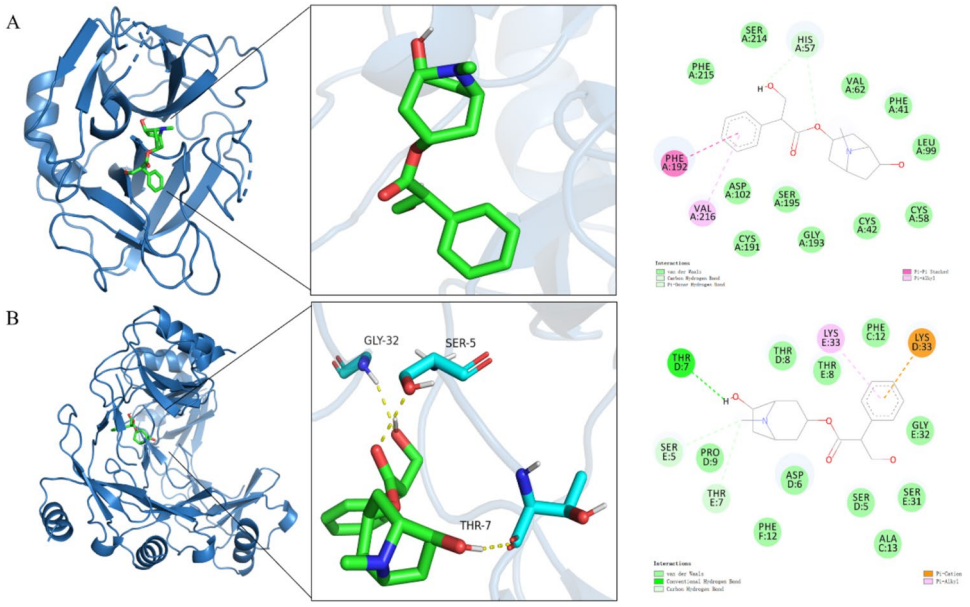

Fig. 17. Molecular docking results. (**A**) Molecular docking analysis reveals a binding affinity of –6.1 kcal·mol^{-1} between Ani HBr and ELANE. (**B**) Molecular docking analysis reveals a binding affinity of –7.6 kcal·mol^{-1} between Ani HBr and CCL5.

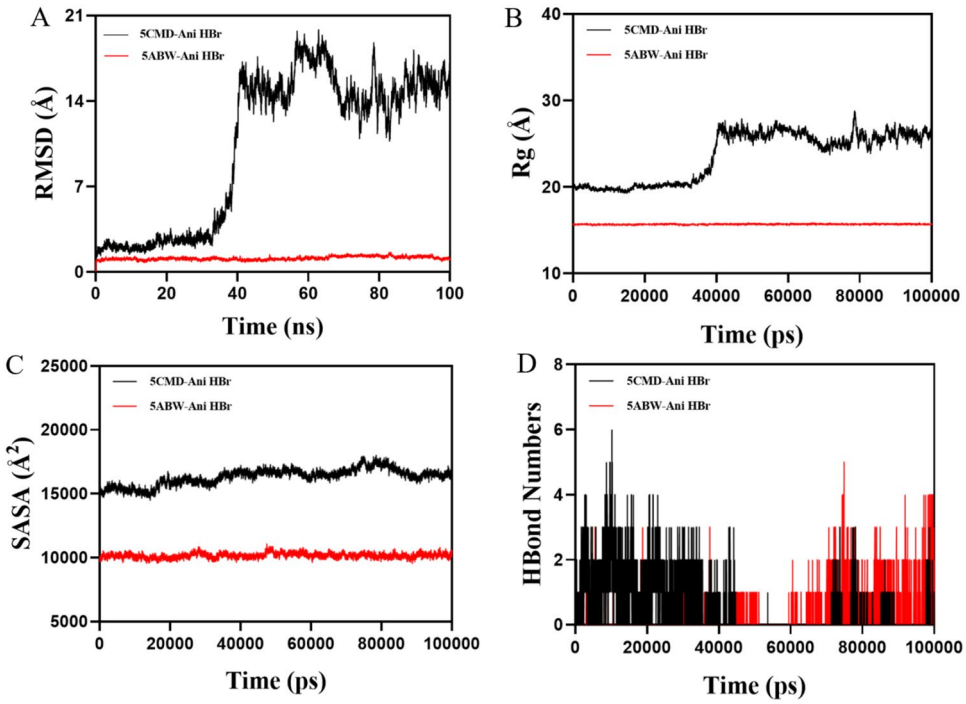

Fig. 18. (**A**) RMSD (root-mean-square deviation) curves indicate backbone stability over time: the black line represents ELANE–Ani HBr, and the red line represents CCL5–Ani HBr. (**B**) Radius of gyration (Rg) profiles over 100 ns showing that the 5CMD–Ani HBr complex remains compact until ~ 35 ns before a modest expansion, whereas the 5ABW–Ani HBr complex maintains a consistently stable and tighter conformation throughout. (**C**) SASA profiles over 100 ns reveal only minor fluctuations for both complexes, stabilizing into plateaus, while Rg data show the 5CMD–Ani HBr complex loosens slightly after ~ 40 ns and the 5ABW–Ani HBr complex remains consistently compact. (**D**) Time-resolved hydrogen-bond counts showing both complexes sustain an average of ~ 2 H-bonds over 100 ns (0–6 for 5CMD–Ani HBr, 0–5 for 5ABW–Ani HBr).

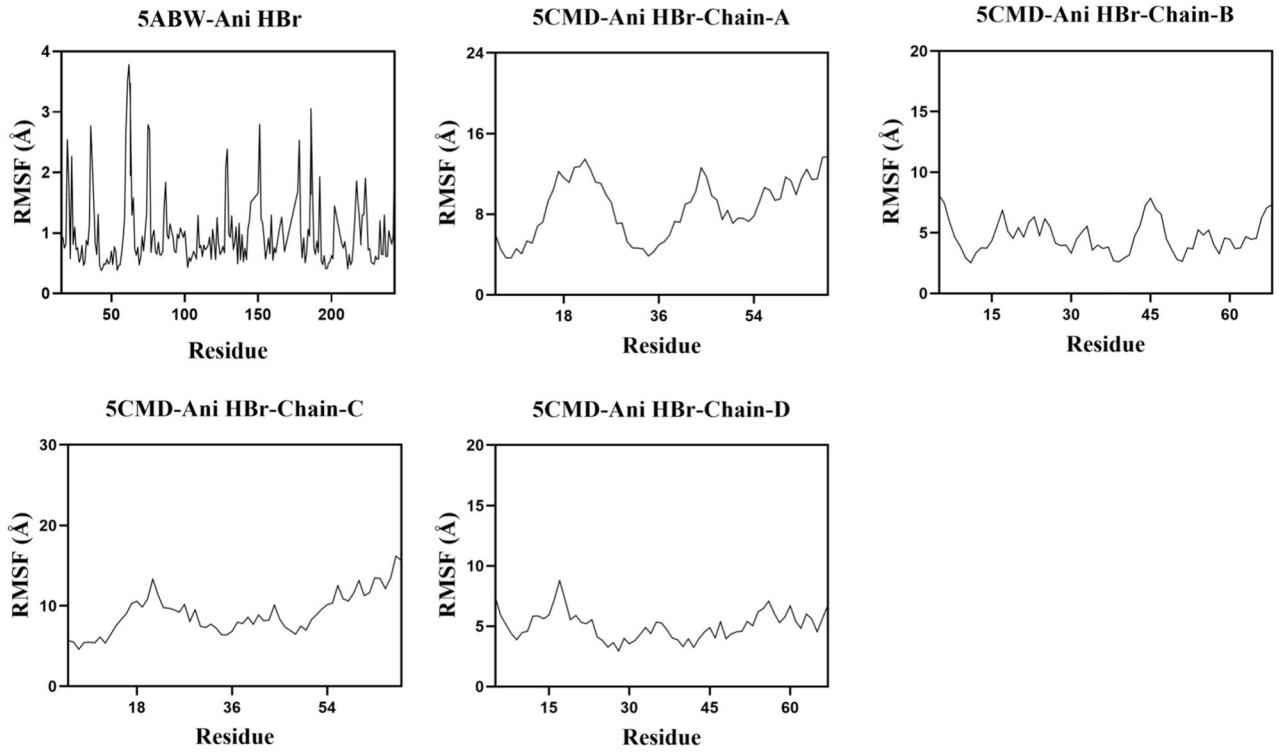

Fig. 19. RMSF plots indicating low residue flexibility (< 0.3 nm) in the 5ABW–Ani HBr complex versus larger fluctuations (up to 1.0 nm) in loop and surface regions of the 5CMD–Ani HBr complex.

the gmx_MMPBSA tool, we estimated the binding free energies of each complex (Fig. 20A). The 5ABW–Ani HBr complex exhibited a ΔG_bind of −13.29 kJ/mol, whereas the 5CMD–Ani HBr complex showed a ΔG_bind of −1.28 kJ/mol. These negative values confirm favorable and spontaneous binding, with the Ani HBr–CCL5 interaction predicted to be particularly strong. Per-residue energy decomposition (Fig. 20B,C) identified SER214, HIS57, PHE192, and SER195 as the major contributors to ELANE binding, and THR7, THR8, PRO9, and LYS33 as key drivers of CCL5 association. Importantly, at the end of the 100 ns simulation Ani HBr remains lodged at the 5CMD dimer interface, forming a hydrophobic contact with ALA9 on chain A and establishing hydrogen bonds with THR3 and THR4 on chain B, and with ASP2 and ASP31 on chain C (Fig. 20D).

Overall, the MD simulations corroborate that Ani HBr forms stable, energetically favorable complexes with both ELANE and CCL5. The exceptional rigidity and low RMSD/Rg of the Ani HBr–ELANE complex, together with its favorable ΔG_bind and key interacting residues, support a mechanistic role for Ani HBr in inhibiting ELANE-mediated NETosis. Concurrently, the strong binding to CCL5 underscores its potential to modulate chemokine signaling in sepsis. These insights lay a molecular foundation for Ani HBr's dual targeting of the ELANE/CCL5 axis in precision sepsis therapy.

Single-cell transcriptomic analysis of the ELANE/CCL5 axis

Cell-type annotation and differential expression

Using CellTypist with a pretrained immune reference model, we annotated clustered cells from GSE175453 into major myeloid and lymphoid lineages (Fig. 21). A majority-voting refinement step based on canonical markers (ELANE/MPO for neutrophils; CD14/CD16 for monocytes; CD3D/E for T cells; NKG7 for NK cells; MS4A1 for B cells) yielded five myeloid subsets (classical monocytes, non-classical monocytes, DC2, pDC, neutrophils), four lymphoid subsets (Tem/effector helper T, Tcm/naïve cytotoxic T, MAIT, CD16$^+$ NK), and minor populations (megakaryocytes/platelets, plasmablasts, late erythroid cells). To assess the impact of Ani HBr–related targets across cell types, we performed Wilcoxon rank-sum tests on 30 intersection genes. ELANE was markedly upregulated in sepsis neutrophils ($p < 0.001$; Fig. 22), consistent with its role in NET formation and pro-inflammatory activation. In contrast, CCL5 expression was elevated across multiple lymphoid subsets—particularly Tem/Temra cytotoxic T cells, CD16$^+$ NK cells, and megakaryocytes/platelets—highlighting its chemotactic function (Fig. 22).

ELANE and CCL5 expression by clinical subgroup

Comparative analysis among healthy controls, RAP, and CCI patients revealed subgroup-specific patterns. ELANE expression was minimal in controls and RAP (Fig. 23A,B) but significantly enriched in CCI neutrophils (Fig. 23C), indicating exaggerated neutrophil activation in chronic critical illness. Conversely, CCL5 was constitutively expressed in CD16$^+$ NK, cytotoxic T, and megakaryocyte/platelet clusters in controls and RAP

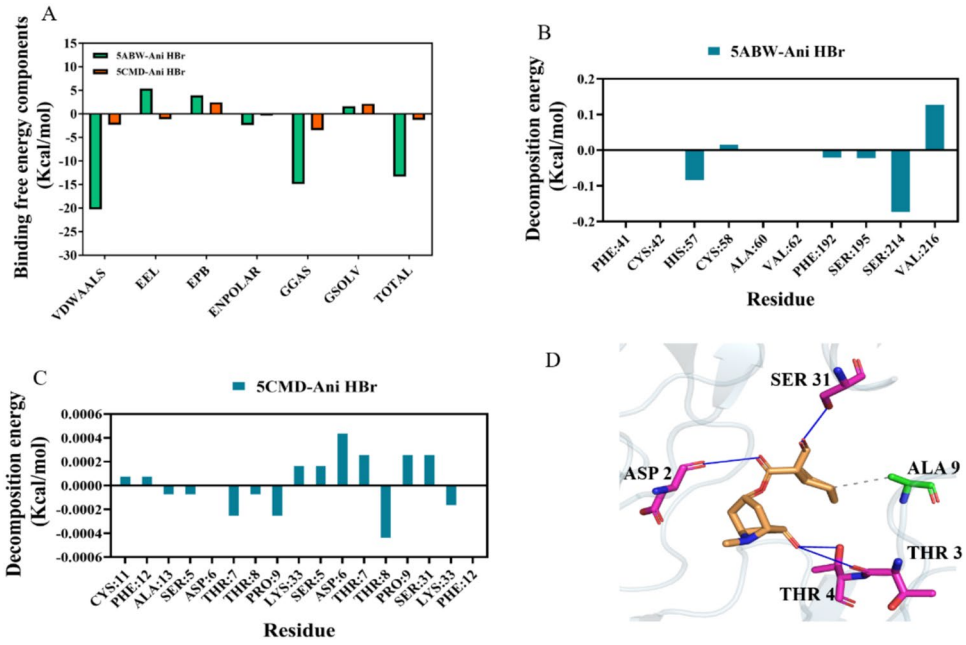

Fig. 20. (**A**) MM-PBSA binding free energies for Ani HBr–ELANE and Ani HBr–CCL5 complexes, showing ΔG_bind values of –13.29 kJ/mol and –1.28 kJ/mol, respectively. (**B**,**C**) Per-residue energy decomposition identifying key contributors: SER214, HIS57, PHE192, and SER195 for ELANE (5ABW), and THR7, THR8, PRO9, and LYS33 for CCL5 (5CMD). (**D**) End-frame view of Ani HBr (orange sticks) at the 5CMD dimer interface. ALA9 (chain A) makes a hydrophobic contact (grey dashed line), and hydrogen bonds (blue dashed lines) form with THR3/THR4 (chain B) and ASP2/ASP31 (chain C).

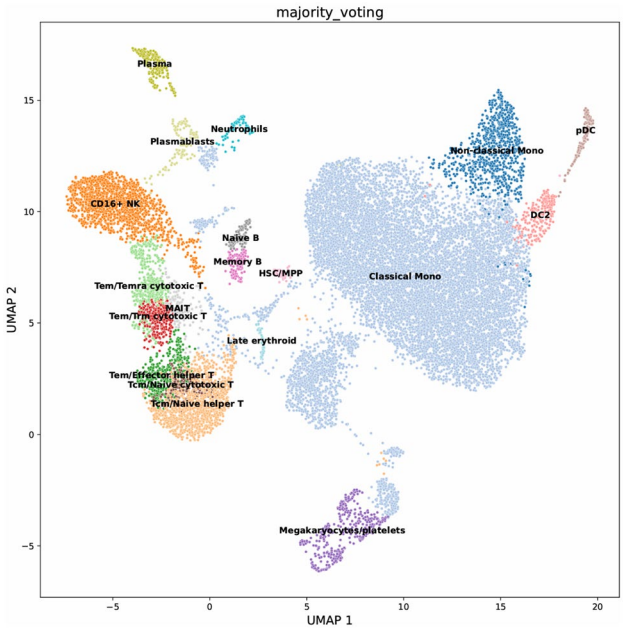

Fig. 21. UMAP Projection and Cell-Type Annotation. UMAP projection of single-cell RNA-seq data showing cluster distributions of major immune cell types and subpopulations. Cells were annotated using a majority-voting strategy: each cell received multiple candidate labels which were consolidated via standardized nomenclature and statistical consensus. Final classification identified five myeloid subsets—Classical Monocytes, Non-classical Monocytes, DC2 (type 2 dendritic cells), pDC (plasmacytoid dendritic cells), and Neutrophils—four lymphoid subsets—Tem/Effector Helper T cells, Tcm/Naïve Cytotoxic T cells, MAIT (mucosal-associated invariant T cells), and CD16⁺ NK cells—and additional populations including Megakaryocytes/Platelets, Plasmablasts, and Late Erythroid cells.

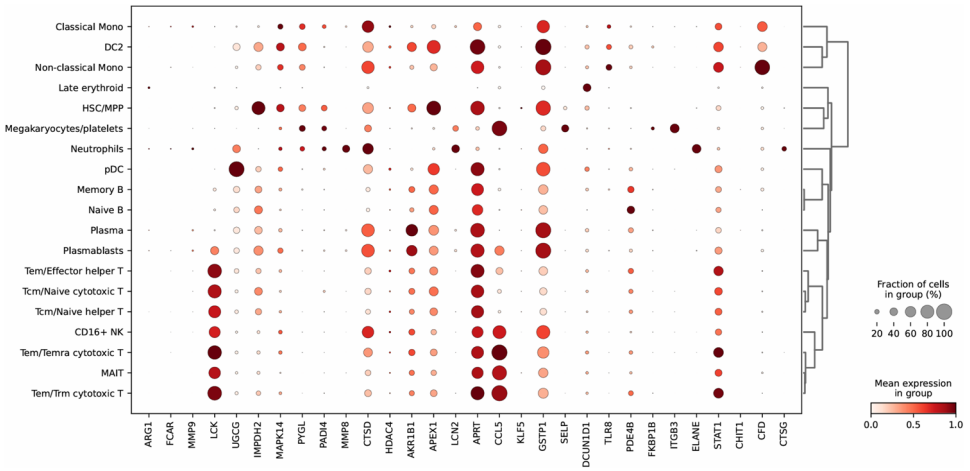

Fig. 22. Differential Expression of Ani HBr–Associated Genes Across Cell Types. Wilcoxon rank-sum tests were performed on 30 genes intersecting Ani HBr targets and sepsis biomarkers to compare expression across annotated cell populations. ELANE is significantly upregulated in neutrophils from sepsis patients, consistent with its pro-inflammatory role and involvement in NET formation. In contrast, CCL5 shows broad upregulation across multiple lineages—including Tem/Temra cytotoxic T cells, CD16⁺ NK cells, and megakaryocyte/platelet clusters—highlighting its central function in chemotactic recruitment. Dot size represents the percentage of cells within each group expressing the gene, and dot color intensity (red) indicates mean expression level.

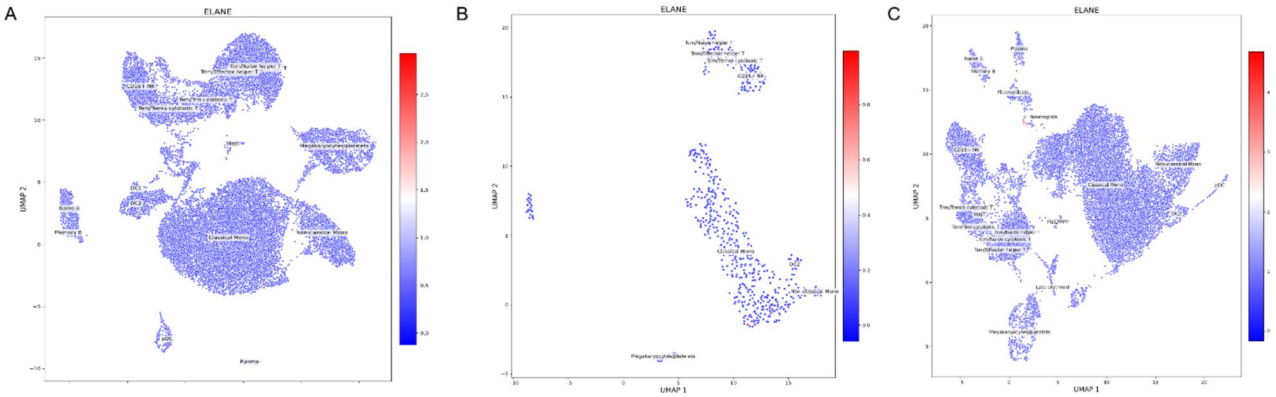

Fig. 23. ELANE Expression Across Cell Types. (**A**) Healthy controls; (**B**) rapidly recovering (RAP) patients; (**C**) chronic critical illness (CCI) patients. Color scale indicates normalized ELANE expression, with blue denoting low and red denoting high expression.

(Fig. 24A,B), but CCI samples exhibited additional upregulation in MAIT and plasmablast populations (Fig. 24C), suggesting amplified chemokine-driven recruitment in severe sepsis.

Pseudotime trajectory analysis

Monocle 3–based pseudotime reconstruction delineated distinct differentiation trajectories in RAP and CCI. In RAP patients, cells progressed from classical monocytes → DC2/pDC → megakaryocyte/platelet → plasmablast/non-classical monocytes → Tem/effector helper T → CD16⁺ NK cells (Fig. 25), with branch probabilities reflecting early innate-immune predominance, mid-stage adaptive-immune engagement, and late regulatory T/NK enrichment (Fig. 26). Notably, CCL5 expression persisted throughout these transitions, suggesting a bridging role between inflammatory and regulatory phases. In CCI patients, trajectories originated from monocytes/HSC-like/megakaryocyte clusters, passed through DC2/pDC, bifurcated into T/NK lineages, and culminated in B-cell states (Fig. 27). Plasma cells and pDCs exhibited the highest lineage commitment, while time-resolved probabilities showed an early bias toward innate lineages, mid-stage T/NK/plasma differentiation, and late B-cell expansion (Fig. 28). ELANE peaked in early myeloid branches, whereas CCL5 remained elevated in megakaryocyte/platelet, Tem/Trm cytotoxic T, and NK clusters, reinforcing an ELANE → CCL5 regulatory axis that may underlie chronic inflammation in CCI.

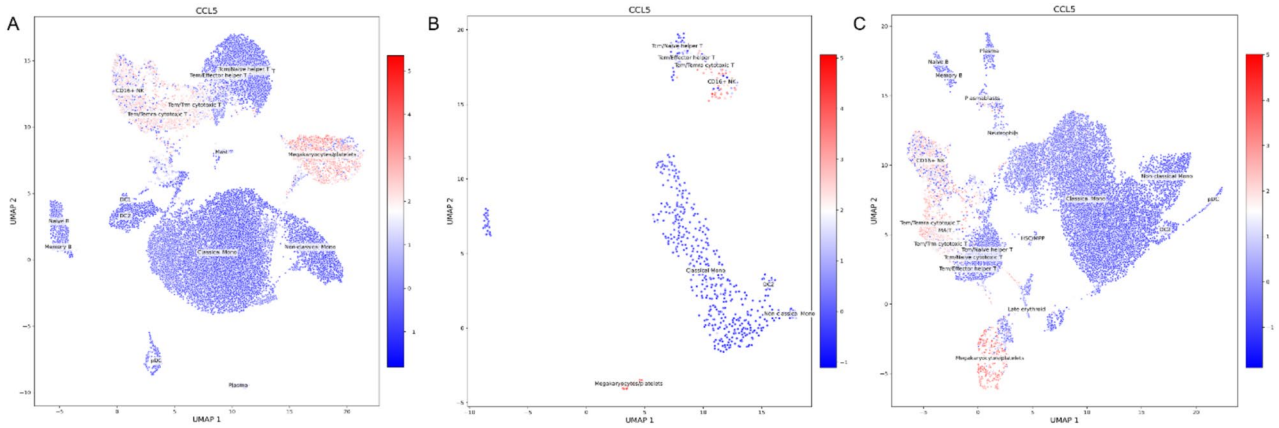

Fig. 24. CCL5 Expression Across Cell Types. (**A**) Healthy controls; (**B**) rapidly recovering (RAP) patients; (**C**) chronic critical illness (CCI) patients. Color scale indicates normalized CCL5 expression, with blue denoting low and red denoting high expression.

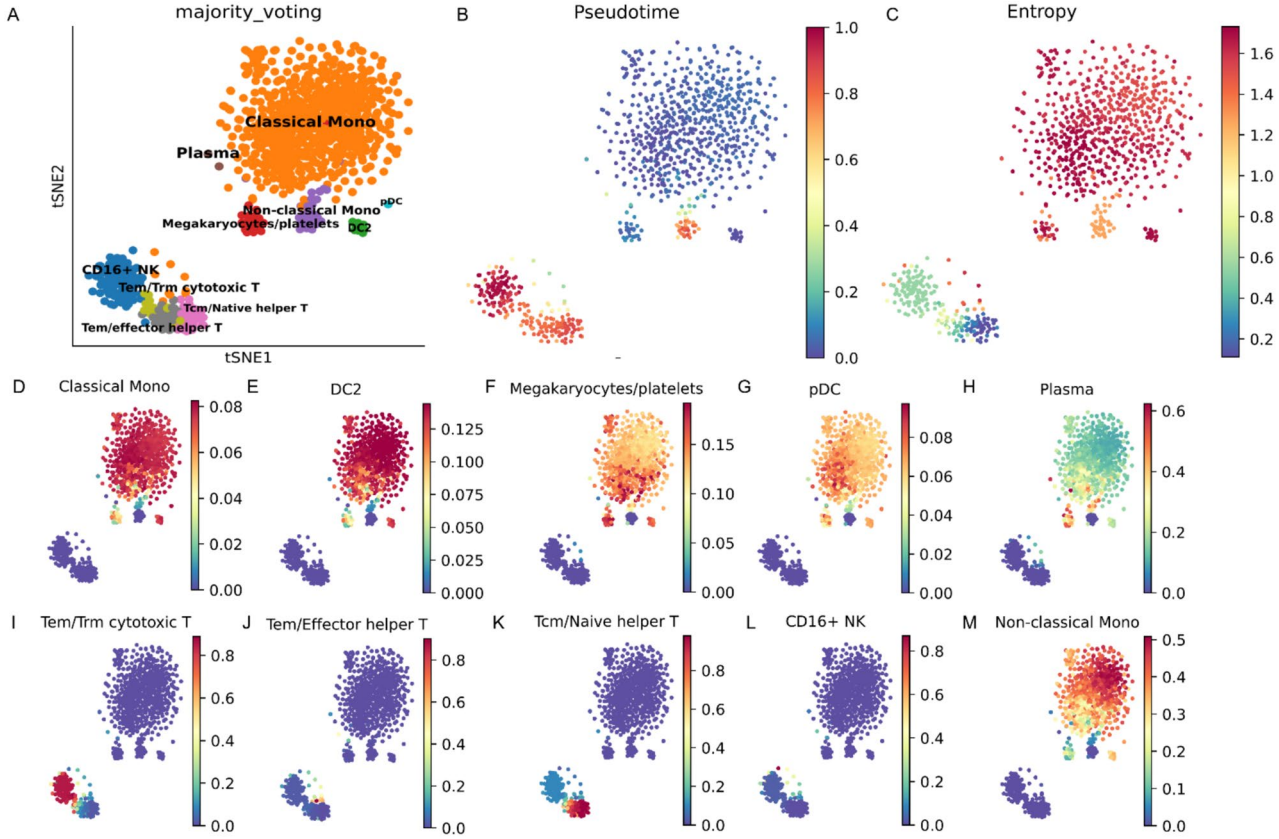

Fig. 25. Pseudotime Trajectory Analysis in RAP Patients. Pseudotime and entropy metrics reveal dynamic state transitions among immune cell types during sepsis in a rapid recovery patient (RAP). (**A**) tSNE plot of immune cells from a rapid recovery patient (RAP), annotated by major cell types using the majority-votingmethod. (**B**,**C**) Cells originate from classical monocytes (Classical Mono), progress through DC2 and plasmacytoid dendritic cells (pDC), then differentiate into megakaryocytes/platelets, plasmablasts, and non-classical monocytes, before transitioning into T-cell populations and ultimately CD16⁺ NK cells. (**D**–**M**) Ten subpanels depict the probability distributions for each cell's commitment to the ten terminal states, confirming the logical consistency between the designated root population and terminal differentiation outcomes. Pseudotime: inferred progression order; Entropy: measure of cell-state diversity.

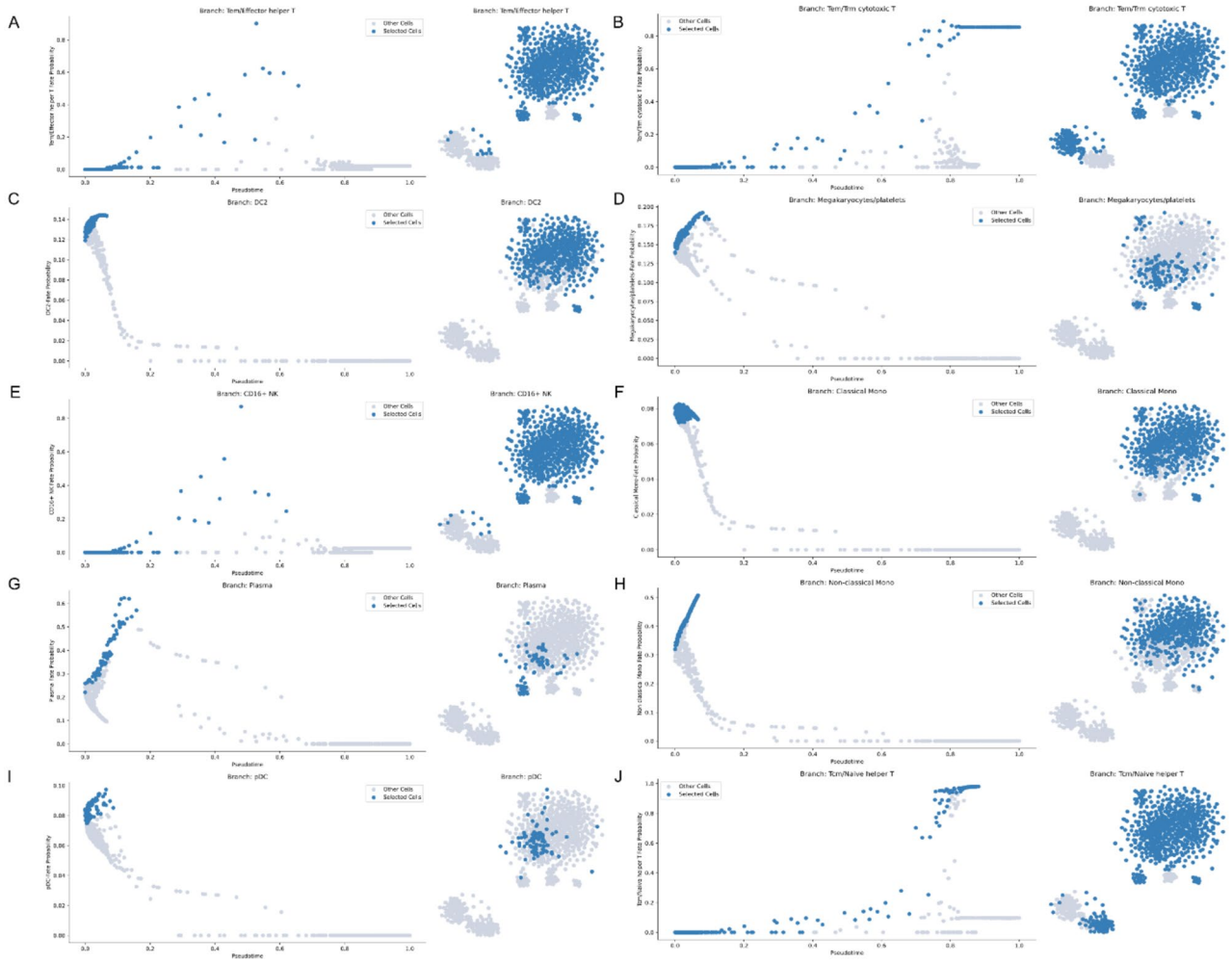

Fig. 26. Dynamic Differentiation Probabilities in RAP Patient Along Pseudotime. Fate probability represents the predicted likelihood of each cell to differentiate into a given terminal subcluster, with higher values indicating stronger commitment. "Selected Cells" highlights the target lineage, contrasted against "Other Cells" to emphasize lineage specificity. Panels **A**–**M** depict how differentiation probabilities evolve over pseudotime: during the early phase (**D**,**F**,**H**), cells primarily commit to monocytes and megakaryocytes/platelets, reflecting innate immune dominance; in the mid phase (**A**,**E**), commitment shifts toward Tem/effector helper T cells and CD16⁺ NK cells, indicating adaptive immune engagement; and in the late phase (**B**,**J**), Tem/Trm cytotoxic T cells and Tcm/naïve helper T cells predominate, signifying the transition to regulatory and reparative states. Notably, CCL5 expression remains enriched in megakaryocytes/platelets, Tem/Trm cytotoxic T cells, and CD16⁺ NK cells throughout pseudotime, suggesting a sustained chemokine-mediated bridge between inflammatory activation and immune regulation.

Discussion

In this study, we combined network pharmacology, prognostic modeling, molecular docking, molecular dynamics, and single-cell transcriptomics to elucidate the immunomodulatory mechanisms of Ani HBr in sepsis. First, network and machine-learning analyses identified ELANE and CCL5 as core targets, and a prognostic Cox model demonstrated that high ELANE and low CCL5 expression correlate with increased 28-day mortality. Second, molecular docking and 100-ns dynamics simulations confirmed stable binding of Ani HBr to ELANE and CCL5. Third, single-cell RNA-seq analysis revealed that ELANE is selectively upregulated in neutrophils of CCI patients, whereas CCL5 is broadly overexpressed in T cells, NK cells, and megakaryocyte/platelet populations; pseudotime trajectories further delineated an ELANE/CCL5 regulatory axis across immune cell lineages. Taken together, these results support a two-stage mechanism in which Ani HBr first inhibits ELANE-driven neutrophil hyperactivation and subsequently modulates CCL5-mediated chemotaxis, thereby restoring balanced immune responses in sepsis. Our findings provide a molecular framework for precision targeting of the ELANE/CCL5 axis and lay the groundwork for future clinical trials stratified by immune-biomarker profiles.

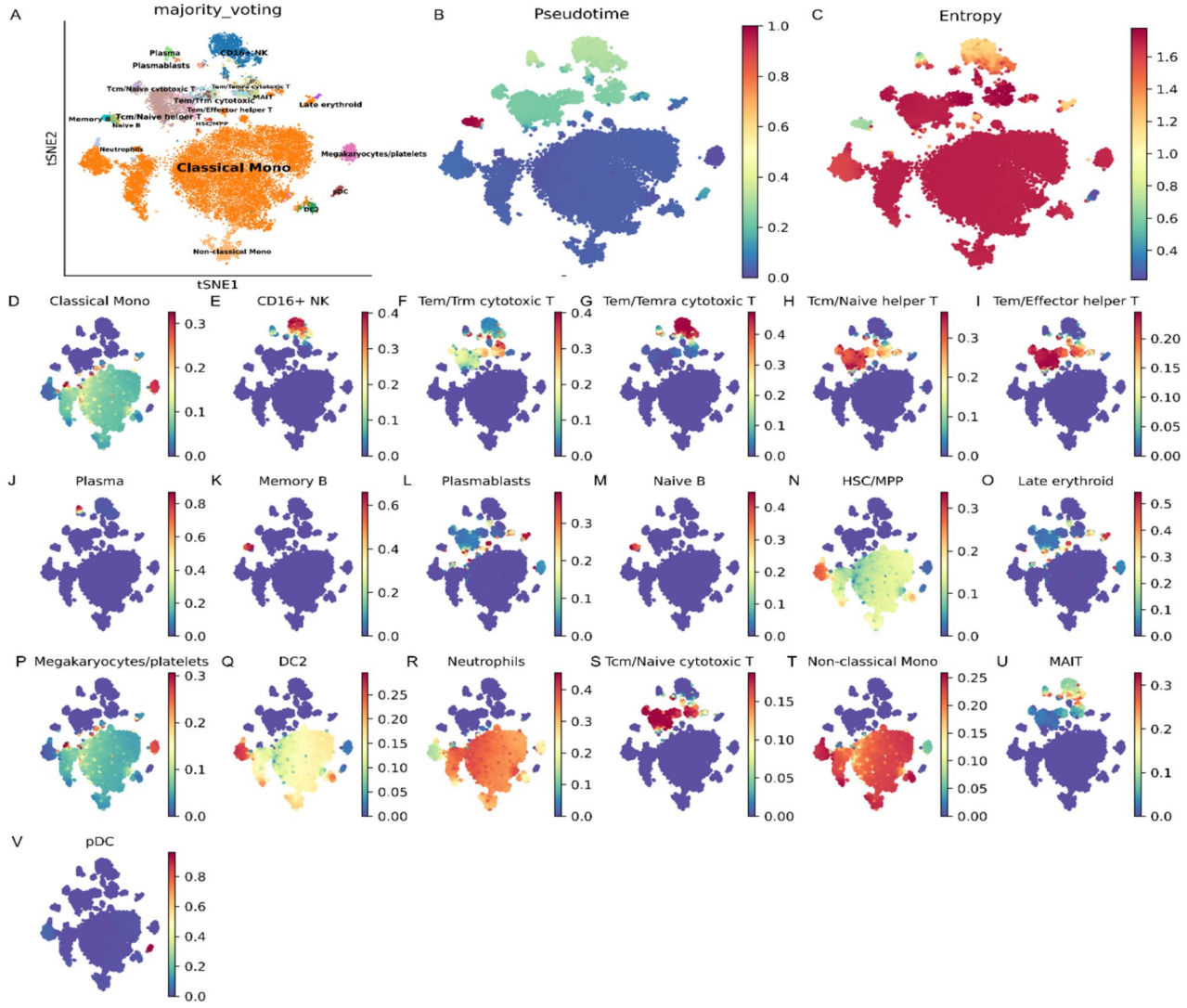

Fig. 27. Pseudotime Trajectory Analysis in CCI Patients. Pseudotime and entropy metrics reveal dynamic state transitions among immune cell types in a chronic critical illness (CCI) patient. (**A**) tSNE plot of immune cells from chronic critical illness (CCI) patients, annotated by major cell types using the majorityvotingmethod. (**B**,**C**) Trajectory origin is traced to classical monocytes, HSC/MPP, and megakaryocyte/platelet clusters, followed sequentially by DC2 and plasmacytoid dendritic cells (pDC), entry into T-cell lineages, differentiation into $CD16^{+}$ NK cells, and eventual maturation into B-cell populations. (**D**–**V**) Panels display probability-based lineage paths from the root to each of the 19 terminal states, with bar plots on the right of each panel indicating fate probabilities. Plasma cells and pDCs exhibit the highest differentiation probabilities (> 0.8), highlighting their dominant roles in immune regulation during CCI.

Ani HBr and microcirculatory regulation in sepsis

Sepsis and Septic shock is characterized by profound microvascular dysfunction, resulting in tissue hypoxia, impaired oxygen delivery, and rapid organ failure[47]. Integrating evidence from in vitro experiments, animal models, and clinical studies, Ani HBr orchestrates a multifaceted restoration of microcirculatory function—attenuating oxidative stress and inflammation while enhancing myocardial performance and hemodynamics—to establish a robust physiological basis for immune modulation. Mechanistically, Ani HBr preserves endothelial integrity by limiting excessive nitric oxide (NO) production and preventing endothelial injury, thereby normalizing vascular permeability and averting microvascular leakage and tissue edema[48–50]. Concurrently, it inhibits platelet aggregation and microthrombus formation, improving blood rheology to ensure smooth perfusion of the capillary network and optimal delivery of oxygen and nutrients to tissues[50]. Furthermore, Ani HBr upregulates endothelial tight-junction proteins, strengthening the vascular barrier and further stabilizing microcirculatory flow[51,52]. Its potent antioxidant action—through increased superoxide dismutase (SOD) activity—efficiently scavenges excess reactive oxygen species (ROS), mitigating oxidative damage to the endothelium and surrounding tissues[53,54]. Intact microcirculation then facilitates not only adequate organ oxygenation and nutrient supply but also the clearance of metabolic by-products, thereby maintaining local

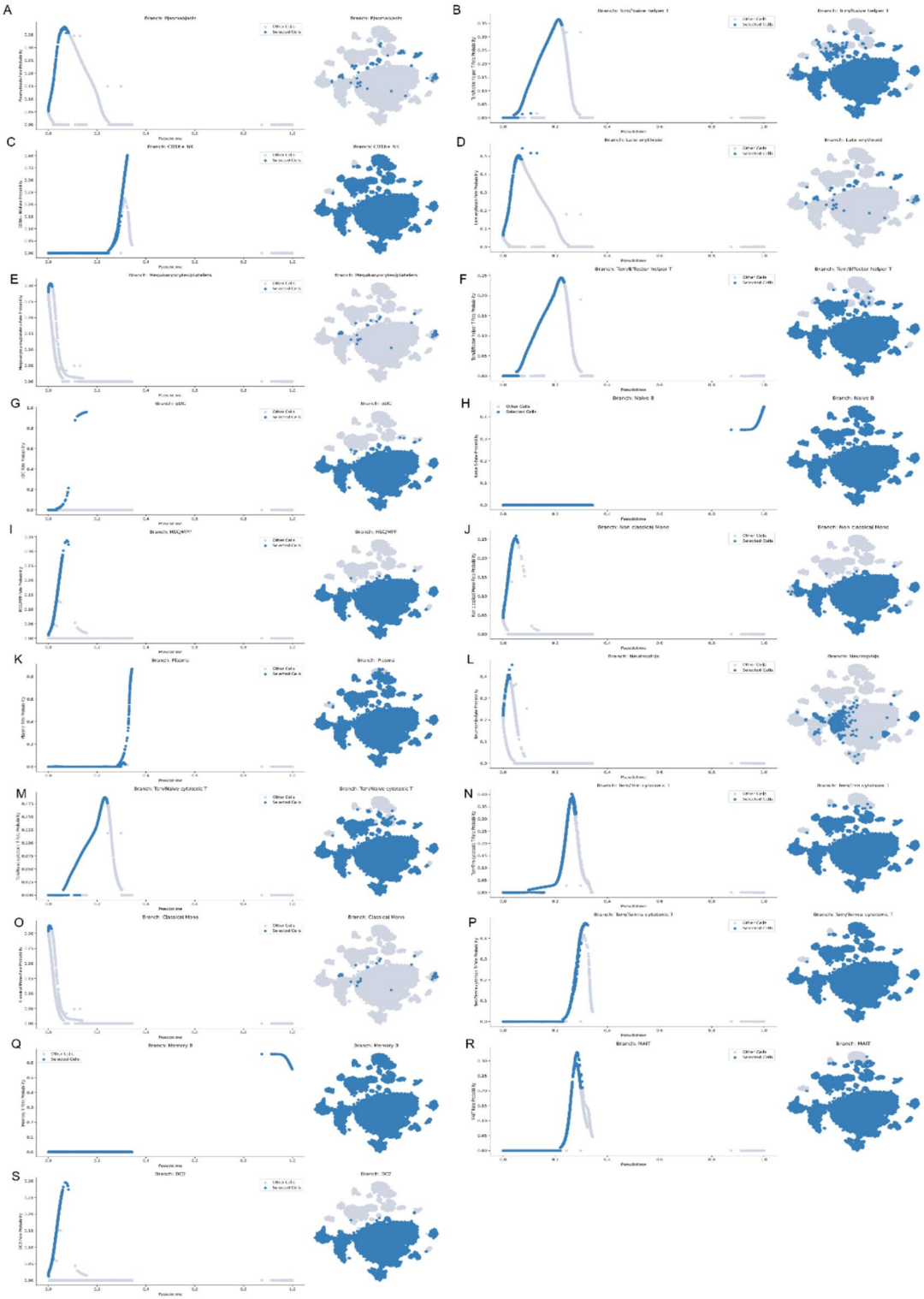

Fig. 28. Temporal Differentiation Probabilities in a CCI Patient. Fate probability denotes the predicted likelihood of each cell differentiating into a given terminal subcluster (higher values indicate stronger commitment). "Selected Cells" highlights the target lineage versus "Other Cells." Across pseudotime, early stages (panels (**O**, **J**, **E**, **S**, **G**, **L**)) show predominant differentiation into monocytes, megakaryocytes/platelets, DC2, pDC, and neutrophils—reflecting a hyperinflammatory response. Mid stages (panels (**B**, **C**, **F**, **K**, **M**, **N**, **P**)) reveal a shift toward T-cell populations, plasma cells, and CD16⁺ NK cells, indicating a transition from inflammation to repair. Late stages (panels (**H**, **Q**)) are characterized by increased B-cell differentiation, marking the onset of antibody-mediated adaptive immunity. Notably, CCL5 expression remains enriched in megakaryocyte/platelet, Tem/Trm cytotoxic T, and CD16⁺ NK clusters throughout, consistent with our model in which Ani HBr sequentially targets ELANE followed by CCL5 to dampen excessive inflammation and promote immune homeostasis.

homeostasis. In contrast, microcirculatory impairment leads to tissue hypoxia and metabolite accumulation, which compromise immune cell function, weaken host defenses, and exacerbate immune dysregulation[55,56]. By restoring microvascular health, Ani HBr creates a permissive microenvironment for immune cell migration, recruitment, and function, thereby underpinning its downstream immunomodulatory effects.

Interplay between microcirculation and the ELANE/CCL5 axis in immune modulation

Microcirculatory impairment in sepsis not only exacerbates hypoxia but also promotes leukocyte sequestration and endothelial injury. Stagnant flow and endothelial activation enhance neutrophil adhesion and degranulation, releasing neutrophil elastase (ELANE) during NET formation[57,58]. Excess NETs—composed of chromatin, histones, and proteases—drive capillary occlusion and disseminated intravascular coagulation, and elevated circulating ELANE correlates with poorer outcomes[59,60]. By downregulating ELANE, Ani HBr disrupts this cycle, limiting NET release, preserving microvascular patency, and protecting against endothelial injury.

Our in silico analyses suggest that Ani HBr binds stably within the catalytic cleft of ELANE, predominantly through hydrophobic and aromatic interactions. The binding site encompasses key residues involved in ELANE's enzymatic activity, and the interaction pattern supports a competitive inhibition mechanism. Specifically, Ani HBr is predicted to occupy the region surrounding the catalytic triad, thereby obstructing substrate access and interfering with enzymatic function. Molecular dynamics simulations further indicate that the Ani HBr–ELANE complex is conformationally stable and energetically favorable, reinforcing the notion that Ani HBr may directly suppress neutrophil elastase activity and downstream NET formation under microcirculatory stress.

Microcirculatory dysfunction markedly disrupts local blood flow, impairs oxygen delivery, and skews the distribution of inflammatory mediators and chemokines, leading to aberrant immune cell localization and function[61]. Under intact capillary flow, a stable CCL5 gradient guides orderly recruitment of monocytes, memory T helper cells, eosinophils, and basophils to sites of infection; by contrast, microvascular dysfunction abolishes this gradient, leading to insufficient effector cell trafficking and exacerbated immune imbalance[62,63]. Moreover, endotoxin tolerance and regulators such as TRIM32 and KSRP dynamically tune CCL5's spatiotemporal expression to balance inflammation with resolution[64,65]. In sepsis, astrocytic adenosine–A1AR activation likewise induces CCL5 release, triggering neuroinflammation and blood–brain barrier disruption, underscoring CCL5's dual proinflammatory and protective roles across organ beds[66].

Docking and simulation results indicate that Ani HBr interacts strongly with the CCL5 oligomer interface, forming a stable and energetically favorable complex. The binding involves both hydrogen bonding and π–cation interactions, particularly at residues associated with receptor binding and oligomerization. This suggests that Ani HBr may interfere with CCL5's ability to engage its receptors or modulate its oligomeric state. Such interference could attenuate aberrant leukocyte recruitment during septic microcirculatory dysfunction. The stable binding dynamics and interaction network support a potential antagonistic or allosteric regulatory role for Ani HBr in modulating CCL5-mediated immune trafficking.

Our single-cell transcriptomic analysis confirms this paradigm: ELANE is nearly undetectable in healthy controls and reversible acute-phase patients but markedly upregulated in chronic critical-illness patients, implicating hypoxia-driven neutrophil hyperactivation when microcirculation fails. Conversely, CCL5 remains highly expressed across all groups but redistributes among cell subsets under severe disease, suggesting compensatory upregulation to offset effector exhaustion. By repairing microvascular integrity and inhibiting ELANE-mediated NETosis, Ani HBr reopens capillaries and halts inflammatory amplification. In this restored microenvironment, its high-affinity, dual-site binding to CCL5 can then fine-tune chemokine-mediated trafficking—promoting protective monocyte and T-cell recruitment while limiting excessive neutrophil influx. This two-stage immunovascular intervention—microcirculatory protection followed by targeted chemokine modulation—addresses the hemodynamic collapse and immune dysregulation of sepsis.

Study limitations and precision medicine prospects

While our findings elucidate a dual Ani HBr mechanism, several limitations must be acknowledged. Our in vivo studies employed specific sepsis models and a single Ani HBr dosing regimen, which may not capture the heterogeneity of clinical sepsis. Immune profiling relied on transcriptomic deconvolution without in vitro or in vivo functional validation of the ELANE/CCL5 axis. Moreover, our clinical cohort lacked real-world single-cell data from Ani HBr–treated patients, precluding direct translational correlations. Future work should include multicenter trials stratified by microcirculatory and neutrophil activation biomarkers, dose–response studies in animal and cellular models, and adoptive T-cell transfer experiments to validate Ani HBr's immunomodulatory effects.

Conclusion

Ani HBr's dual mechanism converges on microcirculatory optimization and immunometabolic reprogramming, including: (1) metabolic reprogramming, which alleviates CCL5 suppression and restores immune cell recruitment; (2) accelerated ELANE clearance, reducing protease-mediated tissue damage; and (3) bidirectional regulation of inflammation, balancing pro-inflammatory and anti-inflammatory responses, and interrupting the vicious cycle of sepsis. This mechanism underscores a triad therapeutic strategy involving vascular repair, metabolic regulation, and immune rebalancing, providing new insights for precision interventions in sepsis.

Data availability

The datasets analysed during the current study are available in the GEO database repository, https://www.ncbi.nlm.nih.gov/geo/query/acc.cgi?acc=GSE65682. https://www.ncbi.nlm.nih.gov/geo/query/acc.cgi?acc=GSE175453

Code availability

The custom code used in this study is available at Zenodo, with https://doi.org/10.5281/zenodo.15340928. The code is freely accessible under the terms of the applicable license, with no restrictions to access. To ensure version control, the code will be maintained in this DOI-minting repository, and future updates will be published as supplementary documents.

Received: 10 February 2025; Accepted: 22 July 2025
Published online: 31 July 2025

References

1. Singer, M. et al. The third international consensus definitions for sepsis and septic shock (Sepsis-3). *JAMA* **315**(8), 801–810. https://doi.org/10.1001/jama.2016.0287 (2016).
2. Hotchkiss, R. S. et al. Sepsis and septic shock. *Nat. Rev. Dis. Primers* **2**, 16045. https://doi.org/10.1038/nrdp.2016.45 (2016).
3. van der Poll, T., Shankar-Hari, M. & Wiersinga, W. J. The immunology of sepsis. *Immunity* **54**(11), 2450–2464. https://doi.org/10.1016/j.immuni.2021.10.012 (2021).
4. Delano, M. J. & Ward, P. A. The immune system's role in sepsis progression, resolution, and long-term outcome. *Immunol. Rev.* **274**(1), 330–353. https://doi.org/10.1111/imr.12499 (2016).
5. Zhang, T. et al. Lactate's impact on immune cells in sepsis: Unraveling the complex interplay. *Front. Immunol.* **20**(15), 1483400. https://doi.org/10.3389/fimmu.2024.1483400 (2024).
6. Kim, Y. J. et al. Ubiquitin regulatory X (UBX) domain-containing protein 6 is essential for autophagy induction and inflammation control in macrophages. *Cell. Mol. Immunol.* **21**(12), 1441–1458. https://doi.org/10.1038/s41423-024-01222-1 (2024).
7. Bai, S. et al. Cardioprotective effect of anisodamine against ischemia/reperfusion injury through the mitochondrial ATP-sensitive potassium channel. *Eur. J. Pharmacol.* **15**(901), 174095. https://doi.org/10.1016/j.ejphar.2021.174095 (2021).
8. Zhang, F. et al. Anisodamine hydrobromide in the treatment of critically ill patients with septic shock: A multicenter randomized controlled trial. *Ann. Med.* **55**(2), 2264318. https://doi.org/10.1080/07853890.2023.2264318 (2023).
9. Xiu, R. J., Hammerschmidt, D. E., Coppo, P. A. & Jacob, H. S. Anisodamine inhibits thromboxane synthesis, granulocyte aggregation, and platelet aggregation. A possible mechanism for its efficacy in bacteremic shock. *JAMA* **247**(10), 1458–1460. https://doi.org/10.1001/jama.247.10.1458 (1982).
10. Du, X. et al. Anisodamine hydrobromide protects glycocalyx and against the lipopolysaccharide-induced increases in microvascular endothelial layer permeability and nitric oxide production. *Cardiovasc. Eng. Technol.* **12**(1), 91–100. https://doi.org/10.1007/s13239-020-00486-8 (2021).
11. Tang, F. et al. Ameliorative effect of anisodamine (654–1/654-2) against myocardial dysfunction induced by septic shock via the NF-κB/NLRP-3 or the PI3K-AKT/NF-κB pathway. *Phytomedicine* **123**, 155277. https://doi.org/10.1016/j.phymed.2023.155277 (2024).
12. Dong, G., Yang, J., Zhao, X. & Mei, X. Study on anisodamine hydrobromide improves Th17/Treg imbalance in resuscitated pigs. *Zhonghua Wei Zhong Bing Ji Jiu Yi Xue* **34**(9), 964–969. https://doi.org/10.3760/cma.j.cn121430-20220117-00066 (2022).
13. Tang, F. et al. Endothelial-derived exosomes: A novel therapeutic strategy for LPS-induced myocardial damage with anisodamine. *Int. J. Biol. Macromol.* **282**(Pt 4), 136993. https://doi.org/10.1016/j.ijbiomac.2024.136993 (2024).
14. Zhao, S. & Iyengar, R. Systems pharmacology: Network analysis to identify multiscale mechanisms of drug action. *Annu. Rev. Pharmacol. Toxicol.* **52**, 505–521. https://doi.org/10.1146/annurev-pharmtox-010611-134520 (2012).
15. Kumar, S. & Sarkar, B. Deciphering the multi-target therapeutic capabilities of Ocimum tenuiflorum Linn. Compounds against systemic lupus erythematosus and inflammatory bowel disease: A network pharmacology and molecular modelling approach. *Nat. Prod. Res.* https://doi.org/10.1080/14786419.2024.2388792 (2024).
16. Ng, S., Masarone, S., Watson, D. & Barnes, M. R. The benefits and pitfalls of machine learning for biomarker discovery. *Cell Tissue Res.* **394**(1), 17–31. https://doi.org/10.1007/s00441-023-03816-z (2023).
17. Zhang, W. Y. et al. Analysis and validation of diagnostic biomarkers and immune cell infiltration characteristics in pediatric sepsis by integrating bioinformatics and machine learning. *World J. Pediatr.* **19**(11), 1094–1103 (2023).
18. Paul, D. et al. Artificial intelligence in drug discovery and development. *Drug Discov. Today* **26**, 80–93. https://doi.org/10.1016/j.drudis.2020.10.010 (2021).
19. Jaiswal, S., Kumar, S., Sarkar, B. & Sinha, R. K. Therapeutic potential of Nelumbo nucifera Linn. in systemic lupus erythematosus: Network pharmacology and molecular modeling insights. *Lupus* **33**(11), 1155–1167. https://doi.org/10.1177/09612033241273074 (2024).
20. Ding, S., Chen, X. & Shen, K. Single-cell RNA sequencing in breast cancer: Understanding tumor heterogeneity and paving roads to individualized therapy. *Cancer Commun. (Lond.)* **40**(8), 329–344. https://doi.org/10.1002/cac2.12078 (2020).
21. Clough, E. et al. NCBI GEO: Archive for gene expression and epigenomics data sets: 23-year update. *Nucleic Acids Res.* **52**(D1), D138–D144. https://doi.org/10.1093/nar/gkad965 (2024).
22. Stelzer, G. et al. The GeneCards suite: From gene data mining to disease genome sequence analyses. *Curr. Protoc. Bioinform.* **54**, 1.30.1-1.30.33. https://doi.org/10.1002/cpbi.5 (2016).
23. Gfeller, D. et al. SwissTargetPrediction: A web server for target prediction of bioactive small molecules. *Nucleic Acids Res.* **42**, W32-8. https://doi.org/10.1093/nar/gku293 (2014).
24. Nickel, J. et al. SuperPred: Update on drug classification and target prediction. *Nucleic Acids Res.* **42**, W26-31. https://doi.org/10.1093/nar/gku477 (2014).
25. Liu, X. et al. PharmMapper server: A web server for potential drug target identification using pharmacophore mapping approach. *Nucleic Acids Res.* **38**, W609-14. https://doi.org/10.1093/nar/gkq300 (2010).
26. Yao, Z. J. et al. TargetNet: A web service for predicting potential drug-target interaction profiling via multi-target SAR models. *J. Comput. Aided Mol. Des.* **30**(5), 413–424. https://doi.org/10.1007/s10822-016-9915-2 (2016).
27. Keiser, M. J. et al. Relating protein pharmacology by ligand chemistry. *Nat. Biotechnol.* **25**(2), 197–206. https://doi.org/10.1038/nbt1284 (2007).
28. National Center for Biotechnology Information. PubChem Compound Summary for CID 118856046, Anisodamine hydrobromide. Retrieved January 28, 2025 from https://pubchem.ncbi.nlm.nih.gov/compound/Anisodamine-hydrobromide (2025).
29. Gene Ontology Consortium. The Gene Ontology resource: Enriching a GOld mine. *Nucleic Acids Res.* **49**(D1), D325–D334. https://doi.org/10.1093/nar/gkaa1113 (2021).
30. Kanehisa, M., Furumichi, M., Sato, Y., Matsuura, Y. & Ishiguro-Watanabe, M. KEGG: Biological systems database as a model of the real world. *Nucleic Acids Res.* **53**(D1), D672–D677. https://doi.org/10.1093/nar/gkae909 (2025).
31. Yu, G., Wang, L. G., Han, Y. & He, Q. Y. clusterProfiler: An R package for comparing biological themes among gene clusters. *OMICS* **16**(5), 284–287. https://doi.org/10.1089/omi.2011.0118 (2012).
32. Szklarczyk, D. et al. STRING v11: Protein-protein association networks with increased coverage, supporting functional discovery in genome-wide experimental datasets. *Nucleic Acids Res.* **47**(D1), D607–D613. https://doi.org/10.1093/nar/gky1131 (2019).

33. Shannon, P. et al. Cytoscape: A software environment for integrated models of biomolecular interaction networks. *Genome Res.* **13**(11), 2498–2504. https://doi.org/10.1101/gr.1239303 (2003).
34. Chin, C. H. et al. cytoHubba: identifying hub objects and sub-networks from complex interactome. *BMC Syst. Biol.* **8**(Suppl 4), S11. https://doi.org/10.1186/1752-0509-8-S4-S11 (2014).
35. Liu, H. et al. Mime: A flexible machine-learning framework to construct and visualize models for clinical characteristics prediction and feature selection. *Comput. Struct. Biotechnol. J.* **29**(23), 2798–2810 (2024).
36. Spytek, M. et al. survex: An R package for explaining machine learning survival models. *Bioinformatics* **39**(12), btad723 (2023).
37. Ning, X. H. et al. Identification of a hypoxia-related gene model for predicting the prognosis and formulating the treatment strategies in kidney renal clear cell carcinoma. *Front. Oncol.* **24**(11), 806264. https://doi.org/10.3389/fonc.2021.806264 (2022).
38. Chen, B., Khodadoust, M. S., Liu, C. L., Newman, A. M. & Alizadeh, A. A. Profiling tumor infiltrating immune cells with CIBERSORT. *Methods Mol. Biol.* **1711**, 243–259. https://doi.org/10.1007/978-1-4939-7493-1_12 (2018).
39. Sturm, G. et al. Comprehensive evaluation of transcriptome-based cell-type quantification methods for immuno-oncology. *Bioinformatics* **35**(14), i436–i445. https://doi.org/10.1093/bioinformatics/btz363 (2019).
40. Bhattacharya, S. et al. ImmPort, toward repurposing of open access immunological assay data for translational and clinical research. *Sci. Data* **27**(5), 180015. https://doi.org/10.1038/sdata.2018.15 (2018).
41. Burley, S. K. et al. RCSB Protein Data Bank (RCSB.org): Delivery of experimentally-determined PDB structures alongside one million computed structure models of proteins from artificial intelligence/machine learning. *Nucleic Acids Res.* **51**(D1), D488–D508. https://doi.org/10.1093/nar/gkac1077 (2023).
42. Jo, S., Kim, T., Iyer, V. G. & Im, W. CHARMM-GUI: A web-based graphical user interface for CHARMM. *J. Comput. Chem.* **29**, 1859–1865 (2008).
43. Mark, P. & Nilsson, L. Structure and dynamics of the TIP3P, SPC, and SPC/E water models at 298 K. *J. Phys. Chem. A* **105**, 9954–9960 (2001).
44. Wolf, F. A., Angerer, P. & Theis, F. J. SCANPY: Large-scale single-cell gene expression data analysis. *Genome Biol.* **19**(1), 15. https://doi.org/10.1186/s13059-017-1382-0 (2018).
45. Domínguez Conde, C. et al. Cross-tissue immune cell analysis reveals tissue-specific features in humans. *Science* **376**(6594), eab15197. https://doi.org/10.1126/science.abl5197 (2022).
46. Cao, J. et al. The single-cell transcriptional landscape of mammalian organogenesis. *Nature* **566**(7745), 496–502. https://doi.org/10.1038/s41586-019-0969-x (2019).
47. Lelubre, C. & Vincent, J. L. Mechanisms and treatment of organ failure in sepsis. *Nat. Rev. Nephrol.* **14**(7), 417–427 (2018).
48. Guo, H. Y., Loren, R. R. & Vanhutte, P. M. Anisodamine inhibits acetylcholine-induced endothelium-dependent relaxation of canine femoral artery. *Chin. Med. J. (Engl.)* **105**(8), 666–670 (1992).
49. Yen, W. et al. Endothelial surface glycocalyx can regulate flow-induced nitric oxide production in microvessels in vivo. *PLoS ONE* **10**(1), e0117133. https://doi.org/10.1371/journal.pone.0117133 (2015).
50. Xiu, R. J., Hammerschmidt, D. E., Coppo, P. A. & Jacob, H. S. Anisodamine inhibits thromboxane synthesis, granulocyte aggregation, and platelet aggregation. A possible mechanism for its efficacy in bacteremic shock. *JAMA* **247**(10), 1458–60. https://doi.org/10.1001/jama.247.10.1458 (1982).
51. Zhang, B. et al. Anisodamine hydrobromide ameliorates acute lung injury via inhibiting pyroptosis in murine sepsis model. *Immunopharmacol. Immunotoxicol.* **46**(5), 662–671. https://doi.org/10.1080/08923973.2024.2386331 (2024).
52. Zhang, Y. et al. Anisodamine enhances macrophage M2 polarization through suppressing G9a-mediated interferon regulatory factor 4 silencing to alleviate lipopolysaccharide-induced acute lung injury. *J. Pharmacol. Exp. Ther.* **381**(3), 247–256. https://doi.org/10.1124/jpet.121.001019 (2022).
53. Qiu, Y. et al. Anisodamine hydrobromide attenuates oxidative stress and proinflammatory cytokines in septic rats induced by cecal ligation and puncture. *Cell Mol. Biol. (Noisy-le-grand)* **68**(12), 54–60. https://doi.org/10.14715/cmb/2022.68.12.11 (2022).
54. Wan, F., Du, X., Liu, H., He, X. & Zeng, Y. Protective effect of anisodamine hydrobromide on lipopolysaccharide-induced acute kidney injury. *Biosci. Rep.* **40**(7), BSR20201812. https://doi.org/10.1042/BSR20201812 (2020).
55. Duranteau, J. et al. The future of intensive care: The study of the microcirculation will help to guide our therapies. *Crit. Care* **27**(1), 190. https://doi.org/10.1186/s13054-023-04474-x (2023).
56. Augustin, R. C., Delgoffe, G. M. & Najjar, Y. G. Characteristics of the tumor microenvironment that influence immune cell functions: Hypoxia, oxidative stress, metabolic alterations. *Cancers (Basel)* **12**(12), 3802. https://doi.org/10.3390/cancers12123802 (2020).
57. McDonald, B. et al. Platelets and neutrophil extracellular traps collaborate to promote intravascular coagulation during sepsis in mice. *Blood* **139**(6), 952 (2022).
58. Sun, S. et al. Neutrophil extracellular traps impair intestinal barrier functions in sepsis by regulating TLR9-mediated endoplasmic reticulum stress pathway. *Cell Death Dis.* **12**(6), 606 (2021).
59. Tabrizi, Z. A. et al. Multi-facets of neutrophil extracellular trap in infectious diseases: Moving beyond immunity. *Microb. Pathog.* **158**, 105066 (2021).
60. Zhang, H. et al. Ferritin-mediated neutrophil extracellular traps formation and cytokine storm via macrophage scavenger receptor in sepsis-associated lung injury. *Cell Commun. Signal.* **22**(1), 97 (2024).
61. Danese, S., Dejana, E. & Fiocchi, C. Immune regulation by microvascular endothelial cells: Directing innate and adaptive immunity, coagulation, and inflammation. *J. Immunol.* **178**(10), 6017–6022 (2007).
62. Moore, J. E. Jr., Brook, B. S. & Nibbs, R. J. B. Chemokine transport dynamics and emerging recognition of their role in immune function. *Curr. Opin. Biomed. Eng.* **5**, 90–95 (2018).
63. Petrie Aronin, C. E. et al. Migrating myeloid cells sense temporal dynamics of chemoattractant concentrations. *Immunity* **47**(5), 862-874.e3 (2017).
64. OuYang, X. et al. TRIM32 reduced the recruitment of innate immune cells and the killing capacity of Listeria monocytogenes by inhibiting secretion of chemokines. *Gut Pathog.* **15**(1), 32 (2023).
65. Bolduan, V. et al. The mRNA-binding protein KSRP limits the inflammatory response of macrophages. *Int. J. Mol. Sci.* **25**(7), 3884 (2024).
66. Guo, Q. et al. Adenosine triggers early astrocyte reactivity that provokes microglial responses and drives the pathogenesis of sepsis-associated encephalopathy in mice. *Nat. Commun.* **15**(1), 6340 (2024).

Author contributions

Ying Chen and Danlei Weng drafted the manuscript and conducted the statistical analyses. Shi Wei and Shuxing Wei were responsible for data collection. Wenqing Ji and Xiya Wang contributed to the literature review. Yali Xu and Xiaoman Wang oversaw manuscript revision, quality control, and overall editing. Shubin Guo designed the study, and Xue Mei supervised and managed the entire project.

Funding

The study was funded by the Capital Research on Special Clinical Application (No. Z211100002921061).

Declarations

Competing interests
The authors declare no competing interests.

Additional information
Supplementary Information The online version contains supplementary material available at https://doi.org/10.1038/s41598-025-13187-w.

Correspondence and requests for materials should be addressed to X.M. or S.G.

Reprints and permissions information is available at www.nature.com/reprints.

Publisher's note Springer Nature remains neutral with regard to jurisdictional claims in published maps and institutional affiliations.